Sea Ice Mapping in Labrador Coast with Sentinel-1 Synthetic Aperture Radar Imagery

by

Weikai Tan

A thesis

presented to the University of Waterloo

in fulfillment of the

thesis requirement for the degree of

Master of Science

in

Geography

Waterloo, Ontario, Canada, 2017

Author's Declaration

I hereby declare that I am the sole author of this thesis. This is a true copy of the thesis, including any required final revisions, as accepted by my examiners.

I understand that my thesis may be made electronically available to the public.

Abstract

Sea ice mapping is crucial to Canadian coast, including marine transportation, environmental protection, resource management, disaster and emergency management, especially under current background of climate change. Canadian RADARSAT-2, like other synthetic aperture radar (SAR) sensors, is an essential source for current sea ice mapping in Canada, However, its limited revisiting makes daily ice chart generation challenging. The RADARSAT Constellation project is expected to be launched in 2018, the gap of data availability is expected to be filled with imagery from multiple sources. Sentinel-1, launched by European Space Agency (ESA) in late 2014, is an alternative source for sea ice mapping with comparable capability of RADARSAT-2 in wide swath mode. The main objective of this study is to examine the performance of Sentinel-1 imagery in sea ice mapping with a semi-automated image segmentation workflow.

The methodology consists of two main steps. First, the most significant features in sea ice interpretation were determined using a random forest feature selection method. Second, an unsupervised graph-cut image segmentation is performed.

The workflow was tested on 15 dual-polarized Sentinel-1A Extra Wide (EW) scenes in Labrador coast from December, 2015 to June, 2016, and the results were evaluated on the accuracy of water segmentation. The study found that: 1) GLCM features are effective in distinguishing different ice classes and 6 most important features were selected; 2) the proposed semi-automated workflow is able to segment Sentinel-1 imagery into 3 to 8 classes for water identification; and 3) generally Sentinel-1 imagery has similar responses from first-year ice compared with previous sensors, but with a different noise pattern in cross-polarized bands; and the overall accuracy of water identification reached close to 95%.

Acknowledgements

Table of Contents

List of Figures

List of Tables

List of Abbreviations

ASAR	Advanced Synthetic Radar
CART	Classification And Regression Tree
CCG	Canadian Coast Guard
CIS	Canadian Ice Service
CNN	Convolutional Neural Network
DEM	Digital Elevation Model
EM	Expectation Maximization
ESA	European Space Agency
ETVOS	Enhanced Total Variation Optimization Segmentation
EW	Extra Wide
GLCM	Grey-Level Co-occurrence Matrix
GMES	Global Monitoring for Environmental Security
GRDM	Ground Range Detected Medium
IPCC AR4	Intergovernmental Panel on Climate Change 4th Assessment Report
IRGS	Iterative Region-Growing using Semantics
IW	Interferometric Wide
LiDAR	Light Detection and Ranging
MAGIC	Map-Guided Ice Classification
MLP	Multi-Layer Perceptron
MRF	Markov Random Field
NESZ	Noise Equivalent Sigma Zero
NRCS	Normalized Radar Cross-Section
NSIDC	National Snow and Ice Data Centre
OOB	Out-Of-Bag
PCA	Principle Component Analysis
RCM	RADARSAT Constellation Mission
ROFTV	Rudin–Osher–Fatemi Total Variation
SAR	Synthetic Aperture Radar
SM	Strip Map

SNAP	Sentinel Application Platform
SNR	Signal-to-Noise Ratio
SRTM	Shuttle Radar Topography Mission
SVM	support vector machine
TOPS	Terrain Observation Progressive Scan
WGS84	World Geodetic System 1984
WV	Wave

Chapter 1   Introduction

This chapter introduces the purpose of this study. Section 1.1 introduces the current condition of climate change and the need of sea ice map products. Section 1.2 summarizes two main challenges, which became the motivation of this study. Section 1.3 presents three main objectives of the study. Section 1.4 describes the structure of the thesis.

1.1   Study Context

Canada is a country largely affected by ice, with more than 4 million km^2 of Canadian waters covered by ice in winter (Canadian Ice Service [CIS], 2016), close to half of Canada's land area. In the form of sea ice, lake ice, river ice, icebergs and other forms, ice plays an important role in Canadian life in different ways, including marine transportation, fishing, offshore resource management, recreation, local weather, and long-term climate (CIS, 2016). The latter issue has drawn Canada's concern in the Arctic where the current global warming trend is having a direct impact on sea ice.

Arctic sea ice extent has been decreasing rapidly through recent decades (Kinnard et al., 2011; Walsh et al., 2016), with a recorded loss of over 1 million km^2 compared to the historical average from late 20th to early 21st century (National Snow and Ice Data Centre [NSIDC], 2016). As Figure 1.1 shows, the Arctic sea ice is currently experiencing significant loss in 2016 within the time scope of this thesis, even compared with the extent in 2012. In addition to loss of coverage, some evidence of ice thickness reduction has also been observed (Serreze et al., 2007; Kwok and Rothrock, 2009). If the decreasing trend continues under this circumstance, it is possible that perennial ice in the Arctic might vanish in a few decades within several climate models from

Intergovernmental Panel on Climate Change 4th Assessment Report (IPCC AR4) (Wang and Overland, 2012; Notz and Stroeve, 2016).
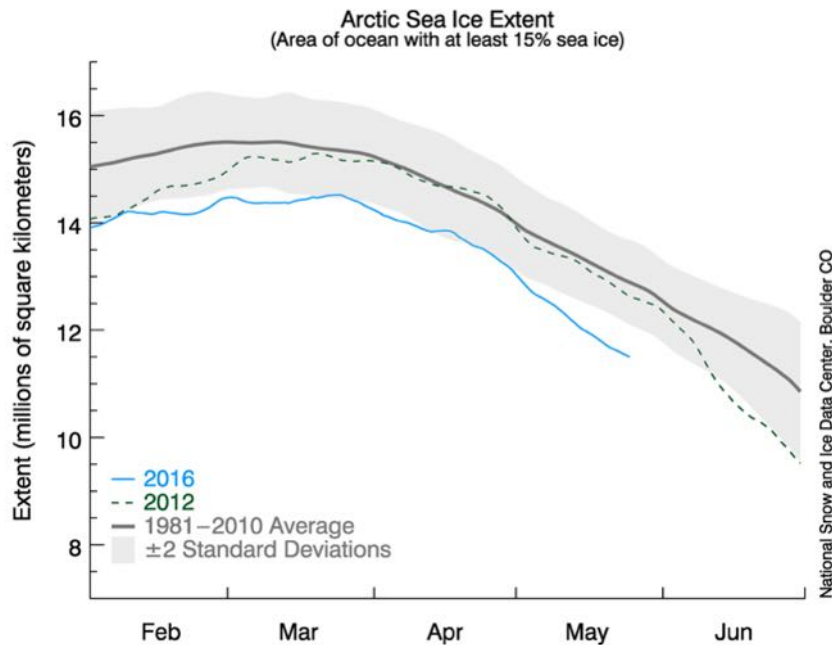
Figure 1.1 Arctic sea ice extent by mid 2016 (NSIDC, 2016)

The continuous loss of sea ice is considered to have profound impacts on Arctic climate, hydrological cycle, and ecology locally, regionally and globally. The loss of sea ice and snow cover in the Arctic has been found to be not only an indicator, but also directly contributing to Arctic Amplification, a phenomenon that near-surface temperature in the Arctic rises much stronger than global average, since the loss of sea ice in summer allows greater warming in upper ocean, while in winter it results in more heat release from the ocean to the atmosphere (Screen and Simmonds, 2010). The decrease of sea ice is also correspondent with Arctic precipitation increase, and they both promotes ocean water freshening, which results in ocean surface salinity anomalies and changes in thermalhaline circulation (Morison et al., 2012). In addition, stronger water vapour and more cloud coverage in Arctic regions would reinforce polar warming, as water vapour is a strong kind of greenhouse gas (Bintanja and Selten, 2014). There are also biological and ecological

consequences as sea ice melt and temperature increase in the Arctic region. Primary producers relying on sea ice such as certain types of algae and phytoplankton account for more than half of the total annual production in the Arctic ocean, but the change of their habitats would result in significant impact in the entire food web. The decrease of sea ice also affects movement, population mixing and pathogen transmission of marine and coastal species such as polar bear, seal and walrus (Post et al., 2013).

In addition to the natural environment, human activities are greatly affected by Arctic sea ice dynamics as well. Marine activities in ice-infested regions such as the Canadian northern and eastern coast, are highly dependent on navigable routes for safety reasons. According to statistics provided by the Canadian Coast Guard (CCG), about 350 ships navigated through the Canadian Arctic in 2013, and the number has been increasing over the past two decades, tripling the number in 1990 (Office of the Auditor General of Canada, 2014). Major forces driving the increase in number of voyages include northern community growth, resource development expansion and tourism (Office of the Auditor General of Canada, 2014). Moreover, the shrinking of Arctic sea ice may provide longer ice-free periods and more navigable routes, resulting in potential marine traffic increase in the future. Therefore, monitoring sea ice dynamics not only helps Arctic climate studies, but also provides valuable resources for safe and efficient ship navigation on the Canadian coasts.

1.2 Motivations

Given the significant impact of sea ice on climate and human activities, it is crucial to monitor sea ice extents and conditions in a timely and accurate manner. Because of the large extent and rapid-changing nature of sea ice, earth observations satellites are invaluable sources for sea

ice mapping. Optical sensors are effective in ice mapping due to the high albedo of ice, but they can provide high-quality imagery only in the day-time with little cloud coverage. In contrast, spaceborne synthetic aperture radar (SAR) systems are suitable for sea ice mapping since they are active sensors that can acquire data regardless of solar illumination and atmospheric conditions at certain frequencies. Consequently, they are capable of acquiring routine images even with bad weather or at night, enabling reliable and long-term monitoring of sea ice. In addition, polar regions usually have long cloudy periods which may create temporal gaps for optical sensors (Karvonen, 2014). It has been observed that precipitation in Arctic regions has significantly increased during the past decades and it may continue to increase due to climate change and sea ice loss (Bintanja and Selten, 2014), which may result in more frequent cloud coverage in Arctic regions in the near future. Therefore, satellite SAR imagery is expected to become the most indispensable source for sea ice mapping in Canada.

CIS, the official provider of sea ice information in Canada, has been using SAR imagery in daily operations for almost 30 years, and the advantages of SAR data became a major driving force in the development of the Canadian RADARSAT-1 program (Arkett et al., 2015). It provided SAR imagery for sea ice mapping in CIS from 1996 to 2013, and RADARSAT-2 has become the major source of imagery since it was launched in 2007 with the major advancement of dual-polarization in ScanSAR mode. There are two major challenges for CIS in current sea ice monitoring using SAR imagery.

First, CIS has been heavily relying on RADARSAT-2 since RADARSAT-1 stopped service in 2013, and RADARSAT-2 has already passed its designed life of service, thus data availability may become a challenge for CIS to generate high quality sea ice products from SAR imagery. Other sources thus need to compensate for this data shortage or potential loss of RADARSAT-2.

Sentinel-1 is a new SAR satellite mission developed by the ESA that provides C-band SAR imagery, consisting of two satellites: Sentinel-1A, launched in April 2014, and Sentinel-1B, launched in April 2016. Sentinel-1 acquires dual-polarized SAR imagery at a wide swath of around 400 km, which is ideal for sea ice mapping. Sentinel-1A has been providing operational data since October 2014, so it would be an important supplementary data source for CIS in addition to RADARSAT-2 currently before the expected launch of RADARSAT Constellation Mission (RCM) in 2018. Most importantly, imagery acquired by Sentinel-1 is open to public without cost. However, Sentinel-1 adopts a new image acquisition technique: Terrain Observation Progressive Scan (TOPS), which is different from ScanSAR as used by RADARSAT-2. Therefore, the challenge is whether Sentinel-1 is able to provide satisfying performance in generating ice products.

Second, CIS received about 64,000 RADARSAT-1 images from 2006 to 2013 and approximately 43,000 RADARSAT-2 images from 2007 to 2014 (Arkett et al., 2015). However, interpretation of images and sea ice product generation still relies heavily on manual processing of experts, and the process is demanding due to the heavy workload. Therefore, an automatic SAR image segmentation and classification system has been in the subject of research at CIS for many years. One of the well-recognized algorithms by CIS is the Map-Guided Ice Classification (MAGIC) software developed by the University of Waterloo (Clausi et al., 2010), and this algorithm is still under development. This algorithm segments SAR images into homogeneous regions and assign labels to these regions with a defined number of classes, but determination of the number of classes still requires interpretation by sea ice experts. Therefore, algorithms that can process SAR imagery automatically or with less human supervision are still in demand.

1.3   Objectives of the Study

The main goal of this study is to explore the effectiveness of sea ice monitoring using Sentinel-1 imagery with a proposed semi-automated image segmentation workflow. Since multi-year ice does not present in the chosen study area of this thesis, the Labrador coast, only first-year ice is investigated in this thesis. To address the aforementioned two challenges in processing SAR imagery of sea ice, the following objectives have been set:

i)   To determine most important features in discriminating different sea ice types in dual-polarized Sentinel-1 imagery through feature selection,

ii)   To examine the effectiveness of incorporating label cost in energy optimization during image segmentation of sea ice to reduce human intervention, and

iii)   To evaluate the ability of dual-polarized Sentinel-1 imagery in sea ice monitoring

1.4   Structure of the Thesis

The rest of the thesis is organized as follows.

Chapter 2 provides a brief background of SAR imaging, followed by an introduction of the new SAR satellite, Sentinel-1 used in this thesis. It also reviews previous ice classification systems using SAR imagery and describes some background of the proposed method.

Chapter 3 introduces current concerns of the study area, the Labrador coast. A general description of sea ice in Sentinel-1 imagery is shown. Then detailed steps of the proposed method are presented.

Chapter 4 provides the results and evaluation of the proposed method, followed by discussions of the results relating to the objectives.

Chapter 5 summarizes the key findings of the study and provides recommendations for future development of the proposed method.

Chapter 2   Background and Related Studies

This chapter presents background knowledge of this thesis. Section 2.1 provides basic knowledge of SAR imaging. Section 2.2 lists current operating and expecting SAR satellites. Section 2.3 introduces the properties of Sentinel-1 SAR imagery. Section 2.5 summarizes state of the art sea ice classification systems using SAR images. Section 2.6 shows indications of literature on the proposed method. Section 2.7 presents a summary of this chapter.

2.1   SAR Basics

SAR is an active radar system, and its properties can be summarized as follow. First, SAR is able to acquire images in high-resolution (e.g. up to 1 m in Spotlight mode of RADARSAT-2) or in large coverage (up to 500 km in ScanSAR Wide mode of RADARSAT-2), so that it can be utilized in different areas of interest in earth observation. In addition, because of the relative longer wavelength compared to which optical sensors operate at, radar waves can penetrate cloud and haze, making SAR imagery independent from weather conditions. Furthermore, SAR is an active system thus it is capable of acquiring images day and night regardless of sun illumination. Finally, SAR measures backscattered pulses from radar waves, so that properties of targets such as physical structure and electromagnetic properties can be exploited from polarimetric signatures.

A radar system measures radar reflectivity of targets as a function of their position by recording both backscatter signal strength and time delay (Moreira, 2013). The antenna transmits microwave pulses into a beam to a target and some energy is reflected towards the sensor. The backscatter is usually measured as σ_0 (normalized radar cross-section [NRCS] or backscatter coefficient), which is a log function of the energy ratio. The energy ratio is the ratio between the received energy and the energy should have received from an isotropic target. In addition, the time

delay between signal transmission and reception is used to infer the distance between sensor and the target so that the location of the target can be measured. SAR sensors are usually mounted on moving platforms such as aircrafts and satellites, and 2D imagery can be produced by processing backscatters continuously.
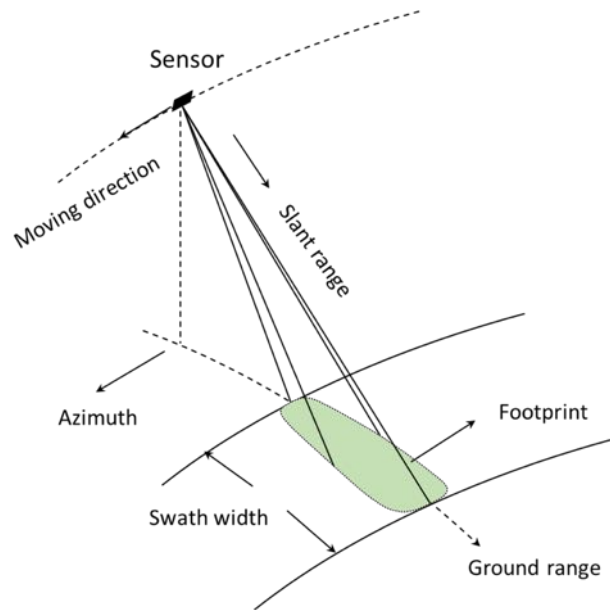
Figure 2.1 SAR imaging geometry, adapted from Eineder and Bamler (2014)

Figure 2.1 shows a typical SAR imaging geometry. Azimuth is parallel to the moving direction of the sensor. Slant range is the distance from the sensor to the target on the ground, while ground range is the distance from nadir to the target. The transmitted pulse forms a footprint on the ground, and the sensor receives responses from all targets within the footprint. The radar sensor distinguishes targets by time differences of echoes in slant range direction, and time differences larger than pulse width can be detected. Accordingly, ground range resolution is a function of slant range resolution dependent on incidence angle. Therefore, SAR sensors have these characteristics: 1) the sensor has to be side-looking in order to increase ground range resolution, 2) slant range resolution and ground range resolution are not dependent on the height

of the sensor, 3) ground range resolution varies across the footprint because of difference in incidence angle (Richards, 2009). In terms of azimuth resolution, a long antenna is synthesized by making use of the motion of moving platform, and azimuth resolution is only related to the length of antenna on board regardless of slant range (Richards, 2009).

Some SAR systems have the capability of transmitting and receiving electromagnetic waves at controlled polarizations, and majority are designed in linear polarization systems, with four typical modes including HH, HV, VV and VH. The letter H stands for horizontal and V stands for vertical polarization, while the first letter indicates the polarization transmits and the second letter indicates the polarization receives by the sensor. By interpretation of polarization signals of targets, physical structure and electromagnetic characteristics could be inferred. In this thesis, HH and HV provided by Sentinel-1 are used.

Although SAR has several advantages over optical sensors, there are still some challenges in processing SAR images. First of all, since SAR systems uses microwave bandwidths, information captured by SAR systems is mostly different from that by optical systems, making acquired imagery unintuitive to interpret. Second, speckle noise is inevitable because of the imaging process of SAR systems, making imagery even more difficult to interpret. Third, radar backscatters are dependent on incidence angle, so that backscatter variations across the scene are usually observed. Moreover, the variations are not only different at different incidence angles (Lang et al., 2016), but also on different surfaces and in different polarization, making it even harder to process large scenes as a whole. These challenges make processing, especially automatic processing of SAR imagery difficult.

2.2   Current and Future SAR Satellites

Satellite SAR sensors have been widely used in ocean and coastal monitoring since the launch of Seasat in 1978, and CIS has been relying heavily on RADARSAT and RADARSAT-2 for operational sea ice monitoring. CIS provides ice information to support marine navigation and coastal operations, and the information can be summarized into two types: strategic and tactical, based on different scales in space and time (Ramsay et al., 1993). Strategic refers to level of detail and requirements for producing daily ice charts, while tactical refers to a higher level of detail for daily operation and ship navigation. From a strategic perspective, the most important information is ice edge location, ice concentration and stage of development, while ice topography, presence of leads and state of decay are more of a concern from a tactical perspective (Ramsay et al., 1993).

In this thesis, sea ice mapping at a small scale is the main objective so that imagery should cover a relatively large area. Some satellite SAR sensors have the ability of acquiring imagery at very wide swath in specific modes. Table 2.1 shows a summary of recent and future satellite SAR sensors that are suitable for sea ice monitoring, and the listed specifications correspond to their imaging modes with largest swath width. Canada is one of the leading countries with possession of advanced satellite SAR sensors, especially C-band SAR, and CIS currently relies on imagery of RADARSAT-2 for sea ice mapping. Sentinel-1 is a C-band satellite SAR mission that has similar specifications in terms of wide swath mapping comparing with RADARSAT-2, so that Sentinel-1 has the potential of providing similar or better performance in sea ice studies. In this thesis, dual-polarized Sentinel-1 EW mode Ground Range Detected Medium (GRDM) products are investigated.

Table 2.1 Recent and future SAR satellites for sea ice monitoring

Satellite	Country	Year	Band	Polarization	Mode	Resolution (m)	Swath width (km)	Revisit time (days)
ERS-2	Europe	1995-2010	C	VV	NA	30	100	35
ENVISAT ASAR	Europe	2002-2012	C	VV/HH	Wide Swath	150	400	30
Sentinel-1	Europe	2014(2016)-	C	HH+HV/VV+VH	Extra-Wide	50	400	12(6)
RADARSAT-1	Canada	1995-2013	C	HH	ScanSAR Wide	100	500	24
RADARSAT-2	Canada	2007-	C	HH+HV/VV+VH	ScanSAR Wide	100	500	24
RADARSAT Constellation	Canada	2018-	C	HH+HV/VV+VH/HH+VV/Compact	Low resolution	100	500	4
RISAT-1	India	2016-	C	HH+HV/VV+VH/HH+VV/Compact	Coarse resolution ScanSAR	50	223	25
Gaofen-3	China	2016-	C	?	ScanSAR	?	650	?
ALOS PALSAR	Japan	2006-2011	L	HH/VV	ScanSAR	100	350	46
ALOS-2 PALSAR-2	Japan	2014-	L	HH+HV/VV+VH/HH+VV/Compact	ScanSAR	100	350	14
COSMO-Skymed	Italy	2007(2010)-	X	HH/VV/HV/VH	ScanSAR Hugeregion	100	200	16
TerraSAR-X(TanDEM-X)-PAZ Constellation	Germany/Spain	2007(2010)/2016-	X	HH/VV/HV/VH	Wide ScanSAR	40	270	11(4/7)
KOMPSAT-5	Korea	2013-	X	HH/VV/HV/VH	Wide Swath	20	100	28

NA: Not applicable; ?: Some technical details of Gaofen-3 is unknown through public sources

2.3 Sentinel-1

The Sentinel satellite constellation is an operational earth observation program developed

by ESA, which is intended to provide systematic and continuous data in a large variety of domains

in earth system, such as land, marine and climate change, meeting the operational and policy needs of the Global Monitoring for Environmental Security (GMES) program (Berger et al., 2012). The Sentinel-l satellite constellation is expected to make substantial contributions in detecting, monitoring and assessing environmental changes (Malenovský et al., 2012). Sentinel-1 provides C-band SAR imagery, which is considered to be particularly effective in cryosphere mapping and monitoring.

Sentinel-1 consists of two satellites equipped with SAR sensors: Sentinel-1A, launched in April 2014 and started providing imagery since October 2014, and Sentinel-1B, launched in April 2016 and just started providing imagery recently. The repeat cycle of a single satellite is 12 days, and it will be reduced to 6 days with both satellites in operation. Four operational imaging modes are provided: Interferometric Wide (IW), Extra Wide (EW), Strip Map (SM) and Wave (WV) (see Figure 2.2a), and EW mode is considered to be preferable in sea ice studies as it has the largest coverage (Malenovský et al., 2012; Torres et al., 2012). Among these imaging modes, IW and EW are collected as TOPS modes (De Zan and Guarnieri, 2006) (see Figure 2.2b) to generate wide swath images of 250km (IW) and 400km (EW) with expected better performance compared to conventional ScanSAR mode (Geudtner et al., 2014) (as illustrated in Figure 2.2c). By steering antenna beam in azimuth direction from aft to fore in addition to range direction, TOPS mode is designed to reduce scalloping effect, as well as keeping ambiguities and signal-to-noise ratio (SNR) constant at azimuth direction (De Zan and Guarnieri, 2006; Geudtner et al., 2014). Sentinel-1 is not only considered to have excellent performance, but also accessible at very low cost as images are open to public by the ESA. The advantages of Sentinel-1 and its similarity to RADARSAT-2 in terms of large swath mapping makes it valuable to CIS as an alternative.
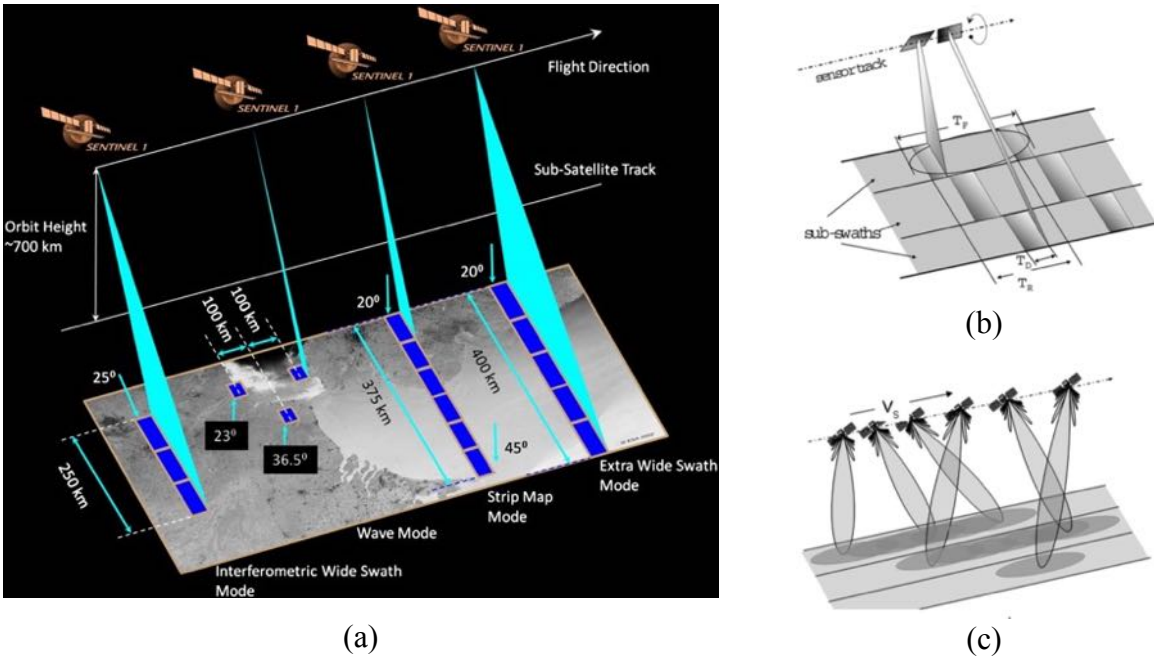
Figure 2.2 (a) Sentinel-1 operational modes (Torres et al., 2012) (b) Sketch of typical ScanSAR scanning mode (De Zan and Guarnieri, 2006) (c) Sketch of TOPSAR scanning mode (De Zan and Guarnieri, 2006)

However, few studies have been published on performance of Sentinel-1 imagery, especially on sea ice mapping, and this becomes one of the motivations of this study. Although Sentinel-1 has similar imaging specifications in EW mode comparing to ScanSAR wide in RADARSAT-2, performance may be different because of the new TOPS image acquisition mode. In addition, because of the new imaging mode, imagery of Sentinel-1 may have different characteristics so that previous methods on RADARSAT-2 imagery may not be applicable or not as effective. Therefore, the performance of Sentinel-1 in sea ice mapping is investigated in this thesis.

2.4   C-band SAR Imaging of First-Year Sea Ice

The understanding of physical characteristics of sea ice is essential in interpretation of radar backscatters. Sea ice majorly consists of ice, brine inclusions, air bubbles, with little solid salt,

which forms an inhomogeneous medium. In most natural conditions, polycrystal structure of sea ice is formed at low temperature, and ice platelets, which are small parallel ice plates, trap seawater in pockets (Nghiem et al., 1995a). As Figure 2.3 shows, the brine inclusions in ice platelets tend to form ellipsoidal shapes and align generally vertically with the c axes parallel to horizontal plane (Weeks and Ackley, 1982). However, the ice platelets are formed with C axes randomly oriented, as depicted in Figure 2.3, except with the influence of underlying sea currents (Nghiem et al., 1995a).
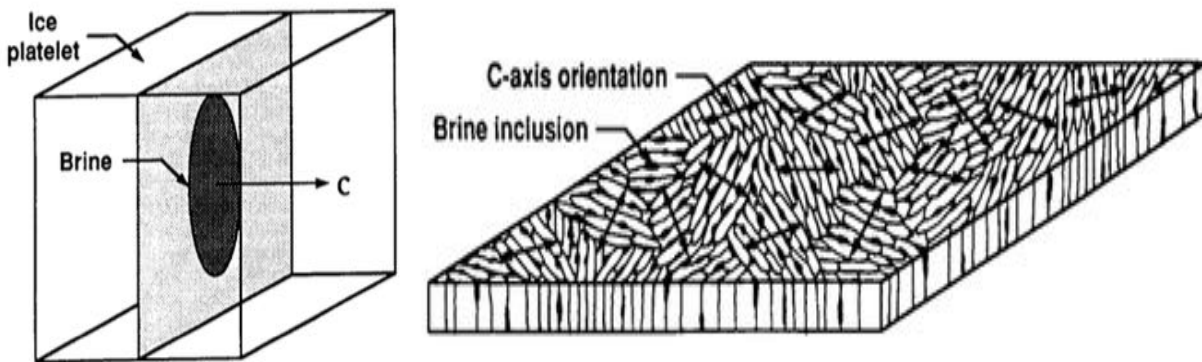
Figure 2.3 Brine pocket in ice platelets and the random orientation in horizontal section of ice

(Nghiem et al., 1995a)

During the growth of sea ice, water contents freeze into the ice platelets, resulting in salinity increase of brine inclusions. The high salinity of brine inclusions results in high permittivity, so that the random orientation of brine pockets makes sea ice anisotropic at vertical directions (Nghiem et al., 1993a). Therefore, the structure of sea ice allows microwave propagation at ordinary and extraordinary directions at different speed and attenuation rates (Nghiem et al., 1995a), especially in first-year ice. Figure 2.4 illustrates the theoretical layered media and scattering mechanism in sea ice. In this thesis, only first-year ice is involved so that the hummock surface does not present. Scattering comes from various sources such as brine inclusion and air

bubbles with different shapes, sizes and permittivity (Nghiem et al., 1995c). However, surface scattering dominates at first-year ice at small incidence angles because of high permittivity contrast at the rough snow-ice interface (Nghiem et al., 1993b; Nghiem et al., 1995a). In addition to first-year ice, ice leads, or very thin ice also present in the images. Ice lead is at an early stage of ice formation, high salinity results in high permittivity contrast at ice surface, leading to larger wave attenuation (Nghiem and Bertoia, 2001). In addition, the presence of brine skim or slush on the top of ice leads may increase microwave attenuation which results in weak volume scattering (Nghiem et al., 1994). Therefore, surface scattering also dominates in ice leads.
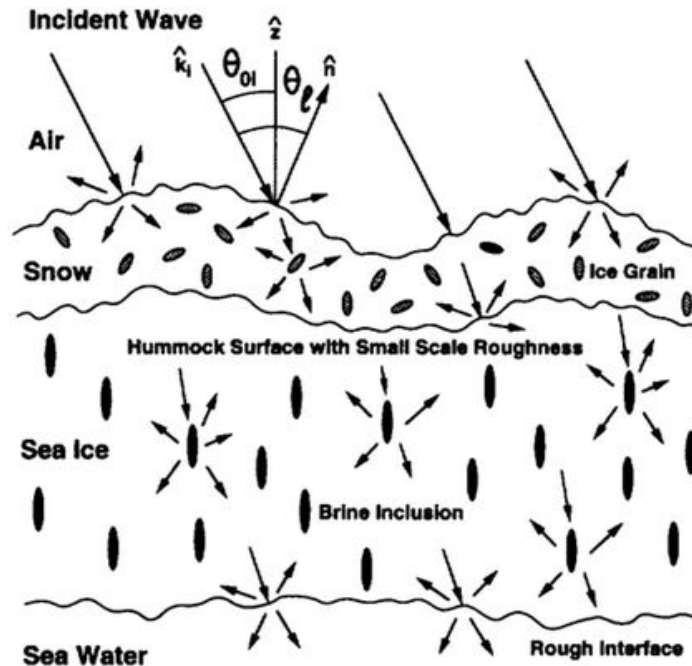
Figure 2.4 Microwave scattering mechanism in sea ice (Nghiem et al., 1995a)

Polarimetric responses of first-year ice and ice leads are found to be similar in previous studies. Figure 2.5 illustrates an average backscatter coefficient of polarimetric response of sea ice during ice formation from a C-band radar scatterometer during fall freeze up in 2003, 2006 and 2007 in Cape Bathurst, in south-eastern Beaufort Sea (Isleifson et al., 2010). In Figure 2.5, FF

stands for frost flowers present on thin ice. Generally, σ_{hh} and σ_{vv} were around -10 dB, and σ_{hv} was around 15 dB lower than the co-polarized band. In addition, variations of response at different incidence angles were observed. Similar results could also be found in other field campaigns (Nghiem and Bertoia, 2001; Nghiem et al., 1995b). However, with the influence of wind, the response of water has a large variation, which may lead to confusion when comparing with ice. With different possible types and structure of first year ice, large variations of polarimetric responses may prevent direct identification of ice types.
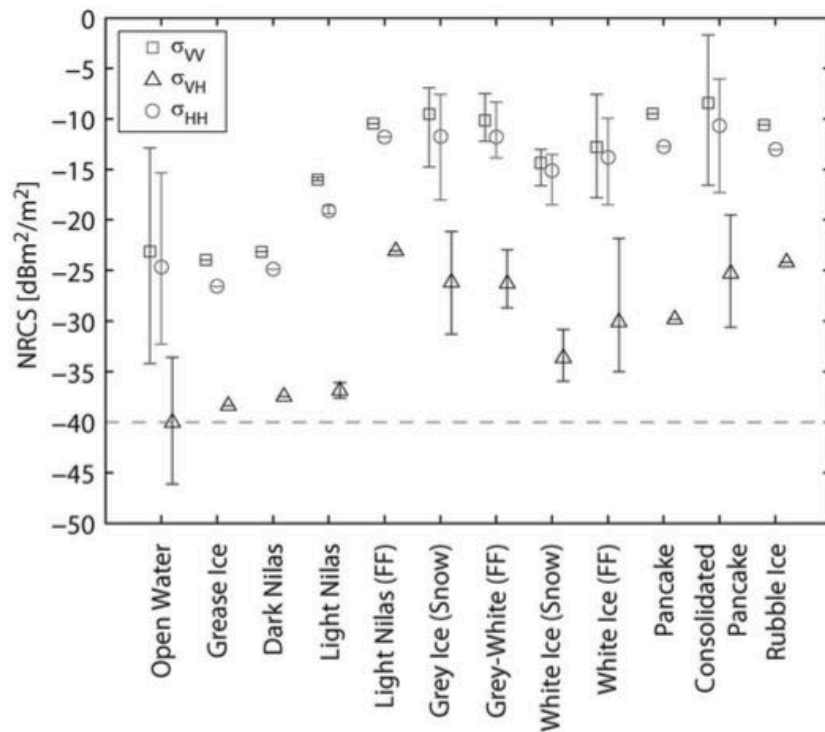
Figure 2.5 Sea ice backscatter coefficients at incidence angle of 30° (Isleifson et al., 2010)

2.5   Previous Sea Ice Classification Systems

Some major publications (limited to the author's knowledge) on sea ice mapping using SAR images in the past five years are summarized and listed in Table 2.2.

Table 2.2 Recent publications on sea ice mapping using SAR imagery

Publication	Data	Polarization	Classes	Target	Method
Ochilov and Clausi, 2012	RADARSAT-1	HH	Depend on egg code, up to 5	Segmentation	IRGS
Yu,et al., 2012	RADARSAT-2	HH, HV	4	Segmentation	MIRGS
Dabboor and Shokr, 2013	RADARSAT-2	Quad	4	Classification	LR
Kwon et al., 2013	RADARSAT-2	HH	4	Segmentation	ETVOS
Zakhvatkina et al., 2013	ENVISAT	HH	5	Classification	NN
Karvonen, 2014	RADARSAT-2	HH, HV	N/A	Concentration	MLP-NN
Leigh et al., 2014	RADARSAT-2	HH, HV	4 for local, 6 for global, 2 final types	Classification	IRGS
Xu et al., 2014	RADARSAT-2	HH	3	Segmentation	K-means
Li et al., 2015	RADARSAT-2	HH, HV	2	Classification	ST-IRGS
Ressel et al., 2015	TerraSAR-X	VV	4	Classification	NN
Wang et al., 2016	RADARSAT-2	HH, HV	N/A	Concentration	CNN

N/A: Not applicable; IRGS: Iterative region-growing with semantics; MIRGS: Multivariate IRGS; LR: Likelihood ratio; ETVOS: Enhanced total variation optimization segmentation; NN: Neural network; MLP-NN: Multilayer-perceptron NN; ST-IRGS: Self-training IRGS; CNN: Convolutional NN.

Table 2.2 shows that traditional pixel-based image classification methods that are still very popular in sea ice image interpretation (Zakhvatkina et al., 2013; Ressel et al., 2015; Karvonen, 2014). Zakhvatkina et al. (2013) used a neural network to classify 20 ENVISAT Advanced Synthetic Radar (ASAR) HH imagery in the Arctic ocean from 2005 to 2008 into five categories, and the overall accuracy in this study reached over 80%. Neural networks were also applied in classifying single-polarized TerraSAR-X sea ice imagery by Ressel et al. (2015). Four scenes of TerraSAR-X ScanSAR with VV polarization taken in April 2013 were used, and the results

reached over 70% and they considered it acceptable. In the study by Karvonen (2014), information provided by HV band in RADARSAT-2 was used as complementary input for the previous ice concentration model developed solely on HH band (Karvonen, 2012). A three-layer multi-layer perceptron (MLP) neural network was trained to estimate sea ice concentration and the error rate of estimation reduced by approximately 20% with the inclusion of HV bands. Besides neural networks, simpler models were still able to provide satisfactory results with proper features generated from SAR images, for example, a KPCA model (Xu et al., 2014) is able to directly finds the most discriminative features.

In addition to traditional pixel-based classification methods, region-based methods involving spatial features have gained popularity in recent years. The MAGIC software (Clausi et al., 2010), which is currently being considered to be adopted by CIS in operational sea ice monitoring (Arkett et al., 2015), is definitely one of the most advanced and popular methods in sea ice image interpretation, in which iterative region-growing using semantics (IRGS) method (Yu and Clausi, 2008) is one of the key components in MAGIC. The IRGS model incorporates edge penalties in a Markov random field (MRF) model, and region growing is adopted in searching for optimal solution (Yu and Clausi, 2008). IRGS firstly over-segments the whole image, and then initial labels are assigned to these segments, and finally adjacent regions having the same labels are merged iteratively until minimum energy is met. The original univariate IRGS used in single polarized SAR images and satisfying results have been achieved (Ochilov and Clausi, 2012), thereafter, IRGS was extended to a multivariate framework (Qin and Clausi, 2010) to utilize multiple polarizations in RADARSAT-2 imagery (Yu et al., 2012). In the study by Leigh et al. (2014), this method was applied in full RADARSAT-2 dual-polarized scenes. A support vector machine (SVM) classifier was trained on 28 features from both HH and HV were used to

distinguish ice and water. After combining ice-water labelling with IRGS, the method tested on 20 images reached over 90% in overall accuracy. Finally, in the most recent study, IRGS was integrated into a self-training framework to reduce manual labeling (Li et al., 2015). In addition to MRF-based methods, expectation maximization (EM) methods can also be applied in other frameworks. For example, an enhanced total variation optimization segmentation (ETVOS) approach has been successfully tested in image segmentation and classification on RADARSAT-2 HH imagery (Kwon et al., 2013).

Moreover, there are more studies that are worth noting in recent years in addition to the two previously illustrated categories. Dabboor and Shokr (2013) explored polarimetric features from quad-polarized RADARSAT-2 imagery and likelihood ratio was utilized in classifying sea ice. Though more polarizations provide significant advantages in interpreting SAR images, the size of each scene of quad-polarized sensors are too small to put into operational use (RADARSAT-2 quad-polarized mode has a swath width of 25km), and the features generated from polarimetric decomposition functions are not applicable in single and dual-polarized images. Deep learning has gained popularity in computer vision and image processing in recent years. Wang et al. (2016) conducted a case study retrieving sea ice concentration using a convolutional neural network (CNN), and the result was comparable to human interpretation. Deep learning methods, which learns image patterns in hierarchy, are revolutionary compared to all the methods mentioned previously, but exhaustive training samples are needed and accurate labelling might not be available.

2.6   Indications of Previous Studies

According to literature, region-based classification methods are considered to be more effective and practical for large-sized SAR images of sea ice. For a typical region-based classification, the following steps can be summarized: 1) SAR image preprocessing, 2) feature extraction, 3) image segmentation, 4) classification. In this thesis, a semi-automated image segmentation workflow is proposed, so that only the first three steps are involved. Some technical details of the listed steps in the aforementioned studies are summarized in Table 2.3.

Table 2.3 Summary of technical details of recent publications

Publication	Method	Image size	Denoise	Incidence angle	Texture	Window size	Feature selection
Ochilov and Clausi, 2012	IRGS	Sample test	N/M	N/M	N/A	N/A	N/A
Yu, et al., 2012	MIRGS	Sample test	N/M	N/M	N/A	N/A	Multiple methods
Dabboor and Shokr, 2013	LR	Sample test	Lee's filter	N/A	N/A	5×5	Literature
Kwon et al., 2013	ETVOS	Sample test	N/M	N/A	N/A	N/A	N/A
Zakhvatkina et al., 2013	NN	N/M	4×4 pixel averaging	Linear function averaged to 25°	GLCM	32×32	Correlation analysis
Karvonen, 2014	MLP-NN	1000× 1000 (est.)	N/M	Linear function averaged to 30° in HH	N/A	N/A	N/A
Leigh et al., 2014	IRGS	2500× 2500	N/M	N/M	GLCM	Multiple	Forward search
Xu et al., 2014	K-means	684×5 44	N/M	N/A	KPCA	3×3	KPCA

Li et al., 2015	ST-IRGS	2000×2000	N/M	N/M	GLCM	Multiple	PCA
Ressel et al., 2015	NN	2200×3000	N/M	Classification on separate beams	GLCM	11×11	Experience
Wang et al., 2016	CNN	1250×1250	N/M	N/M	N/A	41×41	N/A

N/A: Not applicable; N/M: Not mentioned; GLCM: Grey level co-occurrence matrix; PCA: Principal Component Analysis; KPCA: Kernel PCA; est.: estimated

2.6.1 SAR Image Preprocessing

One of the main challenges in interpreting SAR images is inevitable speckle noise. The pixel-based methods usually apply speckle filters to suppress noise during preprocessing. In previous studies, Lee's filter (Dabboor and Shokr, 2013) and enhanced Lee's filter (Kasapoglu, 2014) were applied. Different from pixel-based methods, region-based methods are designed to undermine the influence of speckle noise (Kwon et al., 2013), so that image denoising may not be necessary. Pixel averaging is considered to reduce noise along with reducing image size (Zakhvatkina et al., 2013; Kasapoglu, 2014), since it could be equivalent to a mean filter to some extent. The methods that were able to process full-scene images (Karvonen, 2014; Leigh et al., 2014; Li et al., 2015; Ressel et al., 2015; Wang et al., 2016) all did not include a denoising step, but none of the studies processed the images at full resolution, which means pixel averaging or multi-looking processes had been done initially. The operational sea ice monitoring by CIS does not require processing at full resolution (Scheuchl et al., 2004), therefore reducing image size is reasonable and efficient, and speckle noise can be suppressed. From Table 2.3, state of the art methods are able to handle image size up to more than 2000×2000 pixels (Leigh et al., 2014; Li et al., 2015), while experimental methods used smaller image sizes at around 1000×1000 pixels (Xu

et al., 2014; Wang et al., 2016). Therefore, in this thesis proposing an experimental workflow, image size of approximately 1000×1000 pixels could be considered reasonable.

ScanSAR is adopted in most of the satellite SAR sensors when acquiring wide-swath images, and backscatter variabilities are commonly observed in large scenes, which forms another challenge. For example, in RADARSAT-2 dual-polarized imagery, backscatter intensity decreases as incidence angle increases in HH bands, while HV bands have "banding" effect resulting in differences between swaths. During the preprocessing stage, some of the classification systems took actions to reduce the effect of incidence angle. Some studies performed linear incidence angle correction on the co-polarized band to reduce variations in σ^0 (Zakhvatkina et al., 2013; Karvonen, 2014). Linear relationships can be found between σ^0 and incidence angle, and state of the art methods could be performed in co-polarized bands (Lang et al., 2016). However, the differences vary on different surface, and ground truth is not always available especially before image classification. In addition to co-polarized bands, banding effects in cross-polarized bands also need to be mitigated. Images can be treated by separate beams in order to reduce such effect (Ressel et al, 2015), and a similar technique was applied by Kasapoglu (2014) when retrieving SAR backscatter features. To overcome statistical non-stationarities of each class within a large scene, region-based methods seems to have a better performance. A "glocal" method was put forward to reduce the effect of this problem by segmenting autopolygons at local regions at first, then global IRGS put these segments into more classes (Leigh et al., 2014). However, this method only used HV bands in segmentation, which may ignore some ice signals only found in HH. In more advanced methods such as deep learning, images can be directly processed as whole scenes (Wang et al., 2016). In this thesis, backscatter non-stationarities also exist in Sentinel-1 imagery but with different characteristics because TOPS mode is different from ScanSAR mode in image

acquisition. Therefore, previous methods based on ScanSAR imagery may not be applicable, which makes this study more challenging. In this thesis, the images were not preprocessed specially for dealing with these backscatter non-stationarities to test out the effectiveness of the proposed workflow.

2.6.2   Feature Extraction

Spatial features are considered to be effective in majority of the studies, and among these grey-level co-occurrence matrix (GLCM) features are most popular. However, it is hard to determine which features and what patch/window sizes (if applicable) are most effective in interpreting SAR sea ice images. In the study by Zakhvatkina et al. (2013), visual interpretation was used in determining the window size of 32 and step size of 4. Afterwards, four correlation matrices for four identified classes were compared, and the result indicated that all calculated eight GLCM features were significant in distinguishing these four classes. While in the study of Ressel et al. (2015), correlation was considered to be not as effective as other features, and the window size of 11 was chosen based on experience. In the study by Kasapoglu (2014), 9×9 was chosen as a proper window size in GLCM calculation only based on experience, and a separability measurement based on scatter matrices was conducted to select best features. GLCM was also used in the study by Leigh et al. (2014), candidate features were calculated for window sizes from 5×5 to 101×101 with different step sizes, followed by a forward search feature selection using SVM and 28 features were finally selected. These 28 features can be further reduced to improve computational efficiency using principal component analysis (PCA) (Li et al., 2015). PCA can also be applied in the process of generating features, and KPCA has proved it effective (Xu et al.,

2014). However, since the initial features still need to be calculated, PCA is not able to reduce computation in feature calculation, and the effectiveness of features is unknown after PCA.

In this thesis, GLCM is selected to extract spatial features according to the choices of previous studies. Multiple window sizes and step sizes needs to be calculated, and a feature selection is conducted to determine the most effective features. The GLCM features will not only be calculated on HH and HV, but also cross polarization ratio σ_{HH}/σ_{HV} , which is demonstrated to be effective (Karvonen, 2014). A random forest feature selection method (Genuer et al., 2010) using forward search is applied in producing the most effective feature set in sea ice identification.

2.6.3   Image Segmentation

Previous studies have shown advantages of image segments over pixels. Two image segmentation techniques are illustrated in the previous section: EVTOS , an extension of a Rudin–Osher–Fatemi total variation (ROFTV) optimization (Kwon et al., 2013), and IRGS, a MRF model using region growing (Yu and Clausi, 2008). These two methods have demonstrated the effectiveness of image segmentation in sea ice interpretation. While EVTOS is a presentation of experiment, IRGS has been put into operation and it is able to process full scene images. To the author's knowledge, IRGS can be considered as the most advanced and practical segmentation method in sea ice studies. However, one shortcoming of recent sea ice segmentation techniques is that the number of classes is predetermined before segmentation, and the determination of number of can be tricky. In the latest version of IRGS (Leigh et al., 2014), the images were segmented into autopolygons and 4 classes were determined in each polygon, and in the next step 6 classes were generated using IRGS. In this case, a total of 6 classes were needed in distinguishing two classes:

ice and water. However, the optimal number of classes in different circumstances might not be the same, which is a great challenge when automated processing is needed.

In this thesis, an unsupervised image segmentation method that is able to reduce number of classes is adopted. Similar to IRGS, optimization can also be achieved by graph cut (Boykov et al., 2001), and this method has been extended by adding label cost to reduce number of labels automatically (Delong et al., 2012). With the intension of automatically determining optimal number of labels, this method is selected in this thesis. This method has been widely applied in computer vision, and it has been tested in the field of remote sensing, such as agricultural studies using RGB (Dey et al., 2012; Xu et al., 2013), hyperspectral and SAR imagery (Siva and Wong, 2014), as well as urban studies using Light Detection and Ranging (LiDAR) point cloud (Yan et al., 2014). However, this method has limited applications in SAR imagery, and almost no studies in sea ice could be found. Therefore, the author believes that this label optimization method could be able to provide satisfactory result in sea ice segmentation, and the proposed workflow in this thesis could be one more step approaching automated sea ice classification.

2.7   Chapter Summary

This chapter first summarizes some basic knowledge of SAR imagery, and the new sensor Sentinel-1 is introduced. Then this chapter provides a review of state of the art methods for sea ice studies using SAR images, and the indications of previous studies enlightens the author to produce a semi-automated workflow for sea ice segmentation.

Chapter 3   Sea Ice Mapping with Sentinel-1 Imagery

This chapter presents the methodology of the thesis. Section 3.1 introduces the study site and ice conditions in this area. Section 3.2 illustrates data preparation prior to image segmentation. Section 3.3 elaborates the methodology of the proposed image segmentation workflow. Section 3.4 describes the accuracy assessment process. Section 3.5 summarizes this chapter.

3.1   Study Site

The study site of this thesis is Labrador coast, the mainland part of the Canadian province Newfoundland and Labrador, which roughly locates between 51.9° and 60.6° N, 55.4° and 64.6° W. Labrador Sea and Baffin Bay covers approximately 20% of ice coverage in the northern hemisphere, and it has been found to be one of the regions where sea ice coverage decreases most during the past 30 years (Cavalieri and Parkinson, 2012). Sea ice variability in Labrador Sea has direct impacts on deep convection and atmospheric circulation patterns, which may have profound influence on the climate (Fenty and Heimbach, 2013). Labrador Sea is also an important pass way in marine transportation for Canada since it is one starting point of the Northwest Passage (Ellis and Brigham, 2009). In addition, with the increase of interest in mining and offshore resources in Labrador coastal regions, shipping traffic and offshore operations are expected to increase in the future (Taylor et al., 2015). Therefore, it is of great significance to monitor sea ice conditions in Labrador coast timely and accurately.

The ice regime in Labrador coast is heavily affected by winds and currents, especially by the famous Labrador Current. According to CCG (2012), normally only first-year ice is present during winter time, while on few occasions will old ice occur. Ice usually freeze up before mid-December, and it usually clears out before August. The ice types are mainly new ice and first-year ice, but the

spread of ice from shore varies year to year depending on the low-pressure system present in winter. In this thesis, sea ice in Labrador coast during the winter from late-2015 to mid-2016 was investigated.

3.2   Data Preparation

3.2.1   Data

Table 3.1 List of Sentinel-1 scenes

DatasetID	Date	Acquisition time	Direction
1	2015-12-28	10:27	Descending
2	2016-01-04	10:20	Descending
3	2016-01-11	10:12	Descending
4	2016-01-18	10:03	Descending
5	2016-01-21	10:28	Descending
6	2016-02-04	10:12	Descending
7	2016-02-14	10:27	Descending
8	2016-03-16	10:20	Descending
9	2016-03-23	10:11	Descending
10	2016-04-02	21:41	Ascending
11	2016-04-09	21:33	Ascending
12	2016-04-26	21:40	Ascending
13	2016-05-20	21:40	Ascending
14	2016-05-27	21:34	Ascending
15	2016-06-13	21:42	Ascending

Scenes used in feature selection are shaded in grey

A total of 15 scenes from Sentinel-1A in EW mode were used in sea ice segmentation. The EW mode has the largest scene size in all beam modes of Sentinel-1, with a swath width of

approximately 400 km. The Level-1 Ground Range Detected Medium (GRDM) product was used, which means the products have been focused, multi-looked and projected into the World Geodetic System 1984 (WGS84). The pixel spacing is approximately 40 m by 40 m, and the scene size is approximately 10000×10000 pixels. All the scenes are in dual polarization mode containing HH and HV. Table 3.1 lists the details of the scenes used, and the shaded rows represent those used in feature selection.
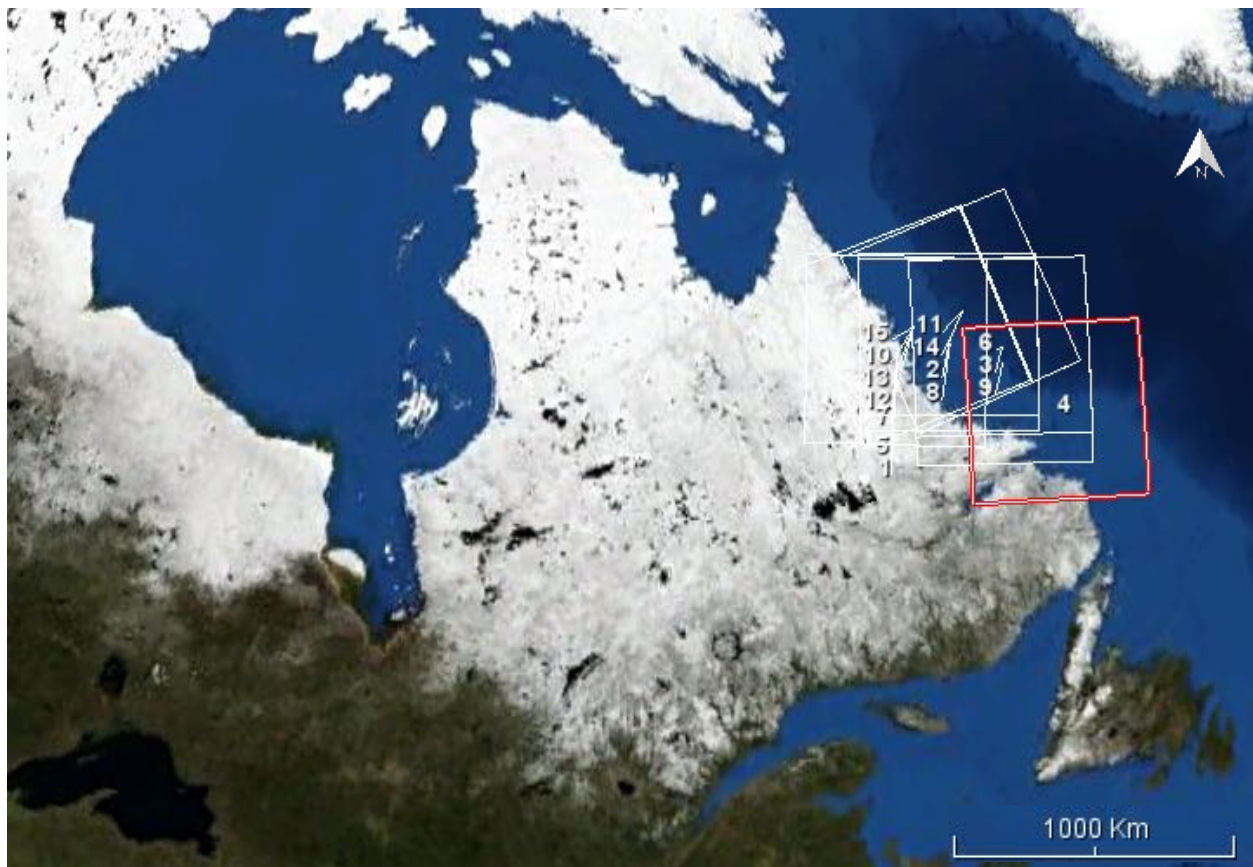

Figure 3.1 Image footprints of Sentinel-1 scenes

Figure 3.1 illustrates the image footprints of all 15 scenes. The images cover coastal regions of Labrador including Canadian territorial sea and exclusive economic zones, where most coastal human activities happen. The highlighted footprint is the scene from January 18, 2016, which is the scene used for illustration purpose in this thesis in later sections.

In addition to Sentinel-1 imagery, ice charts provided by CIS were used to provide ground truth in image classification. The sea ice identification process will be elaborated in Section 3.2.5.

3.2.2   Image Preprocessing

Some preliminary processing has been done during the production of the Sentinel-1 GRDM product, some further processes are needed in this proposed workflow. The preprocessing was done using Sentinel Application Platform (SNAP) software produced by the ESA. Figure 3.2 shows the modules used in the preprocessing step.
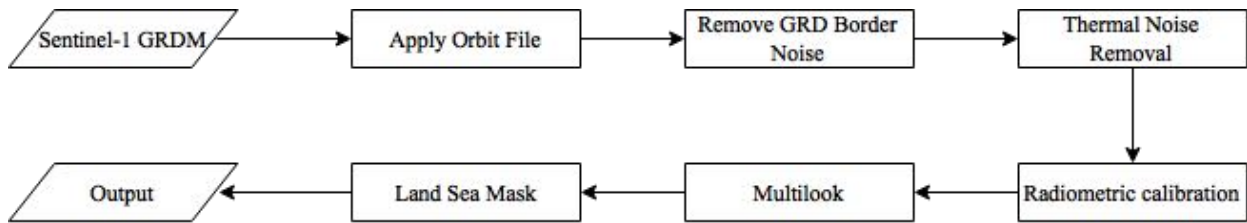

Figure 3.2 Workflow of preprocessing

The first step is to retrieve orbit files from the server. Although the orbit parameters are already in the GRDM products, more precise orbit parameters can be retrieved from ESA approximately two weeks after the generation of Sentinel-1 products. Thereafter, border noise removal was performed since some artifacts may present during the generation of Sentinel-1 GRDM products. And thermal noise was removed according to a look-up-table within the GRDM product. The next step is to perform radiometric calibration, which transforms magnitude into sigma nought (σ_0) values, which is a measurement of radar backscatter on the ground. The magnitude values were transformed in dB scale.

According to literature (Wang et al., 2016; Karvonen, 2014), 1000×1000 would be representative in processing full-scene images for prototype algorithms. The multi-looking process at this stage worked as pixel averaging, and the original image size of 10000×10000 pixels was

averaged by 8 times, resulting in an image size of approximately 1250×1250 pixels. Finally, as the target of interest is sea ice, land regions were masked out using Shuttle Radar Topography Mission (SRTM) Digital Elevation Model (DEM) 3-arc-second (approximately 90 m) product. In addition, the cross-polarization ratio (σ_{HH}/σ_{HV}) is considered effective in sea ice studies using SAR imagery in literature (Karvonen, 2014), so that the ratio was calculated.

Figure 3.3 illustrates the scene captured on January 18, 2016. This scene represents ice conditions in Labrador coast during freeze-up time, and only part of the image is covered by ice. It can be easily identified that the middle part in the scene is covered by ice, and the top left half of the scene is covered by water or very thin ice. Since C-band microwaves has a wavelength of approximately 5cm, very thin ice on top of water may not be distinctive from water in Sentinel-1 imagery. In this thesis, very thin ice is grouped into the class of "water", and "water" used in the following sections may contain part of very thin ice which might not be identifiable. Generally, HV has better contrast between different classes, while HH may capture some characteristics at the surface. For example, in the middle-left part in the image, some structures of ice surface could be found in HH, while in HV those does not present. Thus, both HH and HV contributes to the interpretation of SAR images, and by using only one of them may result in misinterpretation.
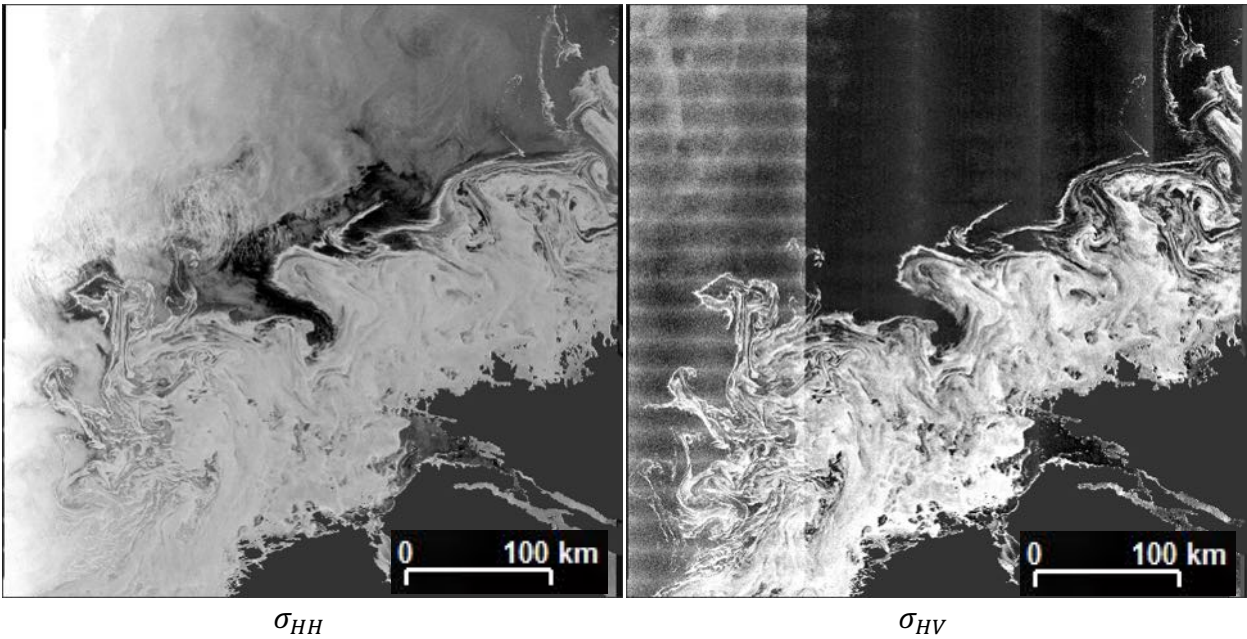
σ_{HH} σ_{HV}

Figure 3.3 Sentinel-1 scene captured on January 18, 2016

3.2.3 Noise in Sentinel-1 Imagery

The noise equivalent sigma zero (NESZ) of Sentinel-1 imagery is around -22dB (ESA, 2016), and values close or below this level could be too noisy to be useful, especially in cross-polarized bands (Dierking, 2010). However, in sea ice studies, water and several thin ice types may be close to the NESZ or even lower, which introduces a challenge for Sentiel-1 image interpretation. Water is the most easily identified class in HV, which has very low backscatters, but has strong banding effects especially in the first sub-swath in. Banding effects also presents in RADARSAT-2 and other SAR images, but backscatters are mostly even within each sub-swath. However, repeating horizontal lines (along look direction) and beam seams in HV (ASF, 2016), especially in the first sub-swath, presents in Sentinel-1 imagery. Currently no consensus has been made on the reason of and solution to this kind of noise, and literature could be hardly found. In these noise-contaminated regions, variations in backscatters from water or other classes having low backscatters, would result in misinterpretation only from σ_{HV} values. Moreover, in HH, water

is largely affected by incidence angle effects, where intensity decrease at a linear pattern from left to right in Sentinel-1 imagery.

Preliminary tests showed that noise in the first sub-swath in cross polarized bands prevents successful identification of ice types and water when full-scene images were processed. Adding that literature could be hardly found on suppression of such noise, it is not feasible to remove the effects of this noise limited to the author's knowledge. Therefore, the first sub-swath was removed as a compromise to reduce the influence of the noise pattern in Sentinel-1 imagery. Such noise also presents in the remaining part of the images, but the variations were observed to be smaller and even across the other swaths. As a result, the image size was further reduced to approximately 915×1250 pixels.

3.2.4   Training Sample Selection

To determine the most distinctive features in identifying different ice types and water, training samples are needed. In this thesis, four scenes were chosen to select training samples for feature selection, and the acquisition dates are January 4, January 18, March 16 and April 2, 2016. In order to select effective training samples, scenes containing most number of ice classes are preferred. Before January, ice just started to form so that few ice classes present, and after April ice started to melt and fewer classes can be identified. The selection of ice classes was based on ice charts provided by CIS, as well as visual interpretation. The ice chart on January 18, 2016 in Labrador coast, as well as how to interpret the egg codes, was shown in Appendix A.

Figure 3.4 shows an RGB composite of the scene on January 18, 2016 and the selected training samples. The scene was not projected so that left and right are reversed compared to the image footprint. From the ice chart, it could be seen that most ice in this scene is covered by grey

ice and grey white ice, while Lake Mellville and top right corner of the image is covered by thin first year ice. In addition, new ice also present at the ice-water boundary. Training samples were selected in small rectangles covering the inferred classes, while complicated regions such as the mid-left part were avoided to assure "purity" of the samples. In addition, the training samples were spread out to cover different incidence angles to capture incidence angle effects. The training samples were selected in ENVI. In this scene, 3163 pixels were selected as training samples. Approximately 3000 pixels were also selected in the other three scenes.
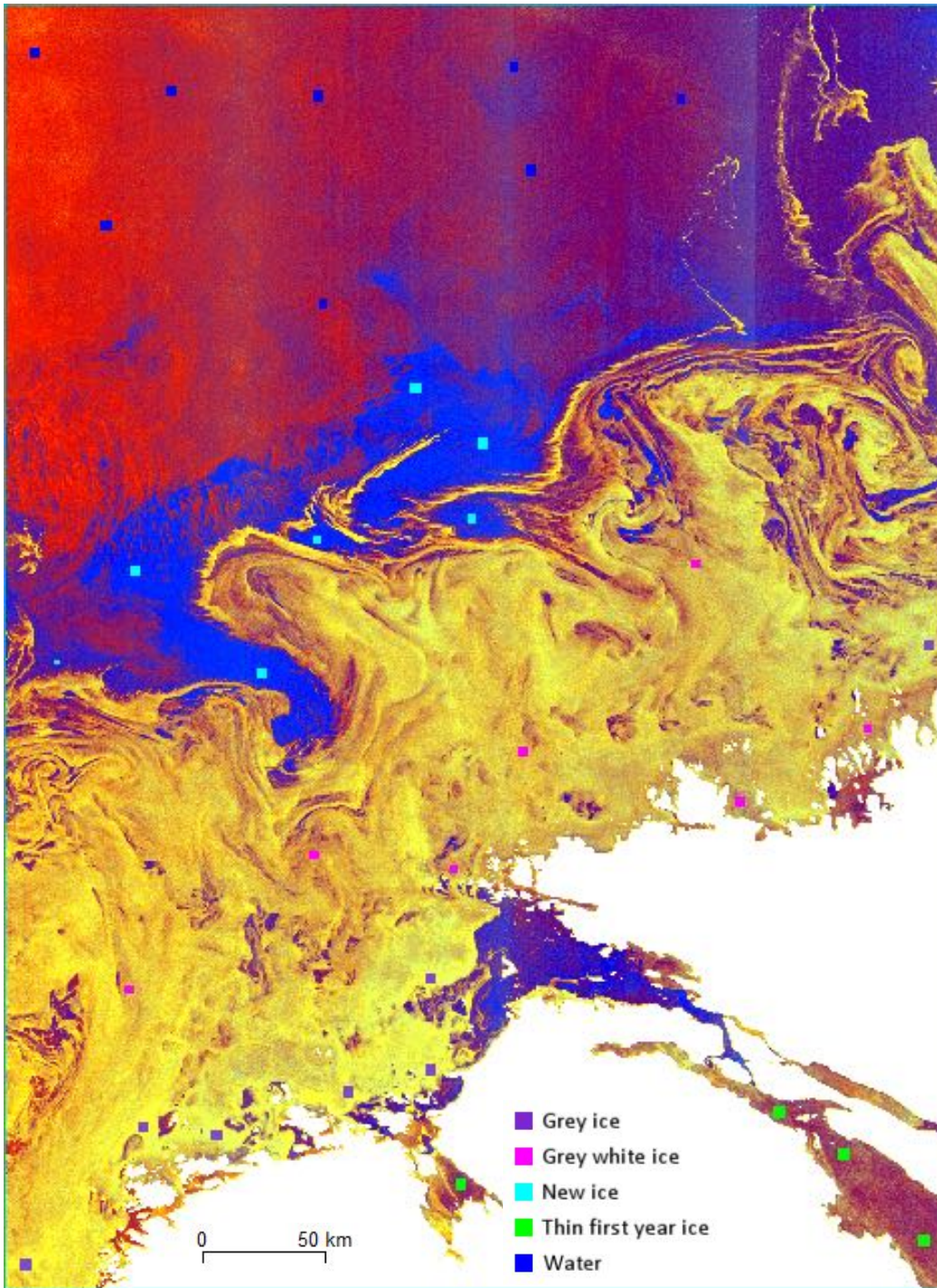
Figure 3.4 Sentinel-1 scene in RGB composite on January 18, 2016 and training samples

(R: σ_{HH}, G: σ_{HV}, B: σ_{HH}/σ_{HV})

3.2.5   Feature Extraction

Spatial features have demonstrated its effectiveness in interpreting remote sensed images, and as previously summarized, GLCM features (Haralick et al., 1973) are the most popular in sea ice images. GLCM probabilities represent all pair-wise combinations of grey levels in the window of interest, and the textures are determined by three parameters: window size, inter-pixel distance and orientation. For window size, several sizes have been chosen for previous studies, but the strategy of feature selection is more reasonable rather than visual interpretation or based on experience. Therefore, a similar scheme to the study by Leigh et al. (2014) was chosen in this study. Since the scene size is around half of that in the study by Leigh et al. (2014), so that 3×3 is added and 101×101 could be dropped. By visual interpretation, 101×101 degrades details of the images too much so that that size was discarded. For inter-pixel distance, or step size, Soh and Tsatsoulis (1999) found that multiple step sizes may be beneficial, and Barber and LeDrew (1991) suggested that 1, 5 and 9 could perform better. In terms of orientation, the look direction is considered to be slightly better in SAR images (Barber and LeDrew, 1991). Adding that a linear decreasing trend was observed between σ_{HH} and incidence angle in water, the look direction was selected in this thesis. In addition to these three parameters, 64 is chosen as quantization of grey scale in all the studies listed in Chapter 2. According to Clausi (2002), quantization larger than 24 should be enough and larger than 64 is not necessary, so that 64 was selected in this study. Eight texture measurements: mean, variance, homogeneity, contrast, dissimilarity, entropy, second moment and correlation were calculated on σ_{HH}, σ_{HV}, and σ_{HH}/σ_{HV}, resulting in a total of 168 candidate GLCM features. The texture features were produced in R using package "glcm" (Zvoleff, 2016). And the texture features as well as the original bands were normalized to 0-255.

Table 3.2 GLCM feature set

Window size (pixels)	Inter-pixel distance (pixels)
3×3	1
5×5	1
11×11	1
25×25	1
25×25	5
51×51	5
51×51	9

3.2.6   Feature Selection

A random forest feature selection method utilizing forward searching (Genuer et al., 2010) was adopted to select the most representative feature. The main idea of random forest (Breiman, 2001) is to combine a number of decision trees, and these trees are built from bootstrap samples in the training set using a random subset of variables. Random forest might be more suitable for feature selection from the author's perspective as it contains an importance comparison during the process. In addition, random forest could have better performance and more computationally efficient compared to SVM (Xu et al., 2014). The feature selection process was done in R using package "VSURF" (Genuer et al., 2016). The feature selection process contains three main steps: 1) thresholding, 2) interpretation and 3) prediction. Detailed description and theoretical basis could be found in the study by Genuer et al. (2010).

In the first step, all the n variables were ranked by variable importance in the descending order, and the least important variables were removed with m variables left. In this case, variable importance is embedded in the random forest classification process, and it's determined by out-of-bag (OOB) error. During the process of random forest classification, each tree t is created from a

subset of training data, while the data not selected are called OOB samples, and the misclassification rate on the OOB samples using tree t is called OOB error ($errOOB_t$). The features are denoted as X and the ith ($i \in [1:171]$) feature is denoted as X^i. To evaluate the contribution of X^i, the values of X^i in sample OOB_t are permuted with random values, and the classification error rate using tree t in this new sample OOB'^i_t is denoted as $errOOB'^i_t$. The difference between the two error rates evaluates how important X^i is in tree t. The importance of variable X^i is defined as:

$$VI(X^i) = \frac{1}{ntree} \sum_t \left(errOOB'^i_t - errOOB_t\right) \tag{3.1}$$

where *ntree* is the total number of trees built in this random forest, and the variable importance is the average error rate difference. The larger the mean error rate is, the variable is more important. All the *n* variables were ranked by average importance through 50 runs and the least important variables were removed based on a threshold given based on a Classification And Regression Tree (CART) model (Breiman et al., 1984) on standard deviation of variable importance. Variables with average importance values lower than the threshold were removed, resulting in *m* important variables.

In the second step, the smallest *k* variables (*k*=1 to *m*) that produced adequately low error rate was selected. It is believed that using all *m* variables leads to the lowest $errOOB$, and the threshold was set as the lowest mean $errOOB$ plus its standard deviation over 25 runs. Random forests were built started from *k*=1 with the most important variable to *k*=*m*, and when the mean $errOOB$ reaches the threshold, the smallest set was determined.

In the third step, based on the importance ranking of the *k* selected variables, an ascending sequence of variables were used to form random forests where only if mean $errOOB$ was

significantly reduced. The threshold is determined by the mean $errOOB$ difference with variables left out at the previous step, as denoted by:

$$Threshold = \frac{1}{m-k} \sum_{j=k}^{m-1} |errOOB(j+1) - errOOB(j)| \qquad (3.2)$$

In this equation, $errOOB(j)$ represents the mean $errOOB$ using j most important variables. The step started from l=1, which is the most important variable, and only if $errOOB(l+1) - errOOB(l)$ was larger than the threshold, the l+1th variable was kept. Thus, less important variables and variables with high correlation could be eliminated. After the three steps, a minimal set of l variables were determined.

During all the three steps, three thresholds can be multiplied by a coefficient considering different circumstances. In this thesis, 168 GLCM features, as well as original bands (σ_{HH}, σ_{HV}, and σ_{HH}/σ_{HV}), with a total of over 12000 samples, were put into feature selection. Since high correlations may exist between GLCM features with different window sizes, adding that only a small set is needed in the image segmentation step, an aggressive parameter selection could improve computational efficiency. The first parameter setting that affects computational speed is *ntree*, the number of trees in random forest. According to the author's previous study (Tan et al., 2015) 20 would be sufficient for SAR image classification. Therefore, 50 was finally chosen to assure consistency of the selection result. Another parameter setting that influences efficiency is that the three thresholds in each step can be multiplied by coefficients. With a larger coefficient, fewer variables would be left in each step. The three coefficients were set according to several testing results, and the selection will be discussed in Chapter 4. Finally, 6 variables, shown in Table 3.3 , were finally selected, and these features were calculated for all 15 scenes to perform image segmentation.

Table 3.3 Six most important features

Most important variables	Rank
σ_{HH} Variance 11×11 step 1	1
σ_{HV} Contrast 25×25 step 5	2
σ_{HV} Mean 11×11 step 1	3
σ_{HV} Correlation 25×25 step 1	4
σ_{HH} Variance 25×25 step 5	5
σ_{HV} Dissimilarity 25×25 step 5	6

3.3 Proposed Image Segmentation Workflow

In this thesis, a semi-automated workflow is proposed to segment full scene Sentinel-1 imagery into desired number of classes. There are three main steps: 1) image preprocessing; 2) feature extraction, and these features were determined by previous feature selection; 3) image segmentation with desired parameter settings. The first two steps were introduced in the previous section as data preparation. The images were calibrated into σ_0 values, and land regions and the first sub-swath were removed. Afterwards, GLCM features were extracted on the preprocessed images, and image segmentation would be performed on these features.

In sea ice studies, because of the large in-class variation of the ice classes, it is difficult to determine the appropriate number of classes in image segmentation to achieve the best result in either supervised or unsupervised methods. For example, water suffers incidence angle effects, adding that the response of water may be different at different wind speeds, so that the variation of backscatter values may be larger than the difference of that between two ice types, such as grey ice and grey white ice. From the perspective of image classification, it might be more appropriate to assign several class labels to one single class with large variations, especially when an

unsupervised method is taken. IRGS (Leigh et al., 2014), the state of the art algorithm, assigns 6 labels to automatically segment one scene into two classes, ice and water. In this thesis, the author intended to propose a workflow that can segment SAR images into more classes, so that selecting an optimal number of classes is crucial. In addition, during winter time there might be five or more ice classes present, while only one or two types of ice appears during freeze-up and melting periods, thus whether one single selection of number of classes can be applicable in different scenes becomes a challenge. In this thesis, an optimization algorithm utilizing label cost, which is capable of determining optimal number of labels dynamically, was chosen to segment the images. The detailed description of this method can be found in the study by Delong et al. (2012).

Image segmentation can be transformed into a multi-label optimization problem, and three costs are taken into consideration: 1) data cost, 2) smooth cost and 3) label cost. The total energy E of a set of label l can be denoted as:

$$E(l) = w_d \cdot \overbrace{\sum_{p \in P} D_p(l_p)}^{\text{data cost}} + w_s \cdot \overbrace{\sum_{q \in N_p} V_{pq} \cdot (l_p, l_q)}^{\text{smooth cost}} + w_l \cdot \overbrace{\sum_{l \subseteq L} h_l \cdot \delta(l)}^{\text{label cost}} \qquad (3.3)$$

where w_d, w_s and w_l stands for the weights of data cost, smooth cost and label cost respectively. These three weights are relative weights, so that w_d was set to 1 in this thesis. A larger w_s promotes smoothness but boundaries between classes may become unclear, and a larger w_l encourages fewer classes but some classes covering small areas may be lost. The final selection of the weights will be discussed in Chapter 4. w_s is referred as scale, while w_l is referred as label cost directly in the next chapter.

Data cost measures how well the assigned label l_p of a pixel p, which minimizes in-class variation of the variables. In this thesis, the cost was defined as the Euclidian distance to cluster centre:

$$D_p(l_p) = \sqrt{\sum (x_p - \mu_l)^2} \tag{3.4}$$

where x_p represents all the values of the 6 variables at pixel p, μ_l represents the mean values of each variable of all pixels with label l.

Smooth cost measures label consistency between neighboring pixels, which reduces typical "salt and pepper" problem in image classification. In this thesis, the 8 adjacent pixels around pixel p were defined as neighbors. A "smoother" segmentation result encourages neighboring pixels to have the same label. If pixel q is within the neighborhood N_p of pixel p, the function V_{pq} penalizes the segmentation if $l_p \neq l_q$. In this thesis, any class could border any other class and no specific priori was defined, so V_{pq} was defined as:

$$V_{pq} = \begin{cases} 1 & l_p \neq l_q \\ 0 & l_p = l_q \end{cases} \tag{3.5}$$

Label cost penalizes excessive number of labels to promote data compactness. The indication function $\delta(l)$ was defined as

$$\delta(l) = \begin{cases} 1 & \exists p: l_p \in l \\ 0 & else \end{cases} \tag{3.6}$$

The order of label l was not pre-set, and each label does not have a specific class name, so that all the labels were given the same penalty if exists by setting the coefficient h_l as 1. During the process of image segmentation, one or more labels might be merged with other labels if a subset l was found in the initial label set L that lead to smaller total energy.

The energy minimization problem with data cost, smooth cost and label cost can be solved using graph cut, a method of partitioning vertices of a graph to achieve energy minimization (Boykov et al., 2001). In this thesis, an extended version of the α-expansion method (Delong et al., 2012) was used to achieve energy optimization. The α-expansion method is able to switch

labels of a large number of pixels simultaneously via graph cut, which results in faster approximation to energy minimization compared to traditional pixel-by-pixel swap. The α-expansion can only be used when the smooth cost function V_{pq} is metric, which means that V_{pq} follows all three conditions: 1) $V_{pp}=0$, 2) $V_{pq}=V_{qp} \geq 0$ and 3) $V_{pq} \leq V_{pr}+V_{rq}$. The workflow of α-expansion used in this thesis is as following: 1) start with initial labeling L, 2) α-expansion on each label in L and find the minimum $E(l)$, 3) if $E(l) < E(L)$, $L=l$, save labeling result and iterate 2) and 3). During this process, some labels may be merged into the α label, and the number of labels could be reduced.

The initial labeling was produced by K-means unsupervised labeling, and the optimization process kept iterating until less than 1% of the pixels changed averaged by the three last iterations, or the number of iterations reached 100. Thus, final segmentation map was produced. The segmentation was done using software "GCoptimization" (Veksler and Delong, 2010) in MATLAB.

3.4   Accuracy Assessment

In order to evaluate the effectiveness of the proposed workflow for sea ice segmentation, an accuracy assessment was performed. Since lack of ground truth for detailed ice classes, it is not feasible to evaluate the segmentation accuracy for different sea ice types. The accuracy assessment can only be performed to evaluate the correctness of distinguishing ice and water using this proposed segmentation workflow.

There are three classes: water, ice and land present in the 15 scenes, and land can be determined by DEM or other maps, thus ground truth for either ice or water is needed. However, after removal of the first sub-swath, only 13 scenes contain water. The ground truth of water was

generated by manual digitization by the author based on the interpretation of SAR images with reference to ice charts provided by CIS. A ground truth image two classes: water and others, was produced for 13 scenes.

The results of image segmentation may contain different number of classes ranging from 3 to 8, and this proposed method does not include a classification step due to sea ice complexity. Therefore, the possible water segments were manually picked and merged, and the others were also merged accordingly. An error matrix (Congalton, 1991) was produced for each of the segmentation scenarios, and overall accuracy, user's accuracy and producer's accuracy of class water were calculated.

Table 3.4 Error matrix for accuracy assessment

| | | Segmentation Results | |
		Water	Other
Ground Truth	Water	A	D
	Other	C	B

The overall accuracy is the ratio between number of pixels correctly labeled and total number of pixels, which evaluates overall performance, and it's denoted as: $(A + B)/(A + B + C + D)$. The user's accuracy of water is the ratio between the number of pixels correctly labeled as water and the number of pixels labeled as water in the results, which evaluates the reliability of the results from a user's perspective, and it's denoted as: $A/(A + C)$. The producer's accuracy of water is the ratio between the number of pixels correctly labeled as water and the number of pixels of water in ground truth, which measures how well water is correctly labeled from a map producer's perspective, and it's denoted as: $A/(A + D)$. These three measurements helped to decide which parameter set produced the best results.

3.5   Chapter Summary

This chapter firstly provided some background of the study area, Labrador coast, as well as current concerns and opportunities in this region regarding sea ice monitoring. Then, the chapter introduced the 15 scenes of Sentinel-1 GRDM products in this study. Afterwards, backscatter characteristics of different types of sea ice in Sentinel-1 imagery were described according to the selected training samples. Finally, the proposed semi-automatic image segmentation workflow was introduced in detailed steps. The results were provided in the next chapter.

Chapter 4   Results and Discussion

In this chapter, the results of each step in the workflow will be displayed. Some uncertainties and limitations of each step will be discussed. Section 4.1 discusses the noise in Sentinel-1 imagery and results of training samples are shown. Section 4.2 shows the results of feature selection. Section 4.3 presents the results of image segmentation, and specific scenes were discussed. Section 4.4 summarizes this chapter.

4.1   Training Sample Selection in Noisy Sentinel-1 Imagery

4.1.1   Noise in Sentinel-1 Imagery

As introduced in Section 3.2.3, backscatters close or below the noise floor show some variations in Sentinel-1 imagery of sea ice and water, and the noise from the sensor may result in misinterpretation of these imagery. The backscatter variance on the surface with lowest values would show some patterns of the noise.
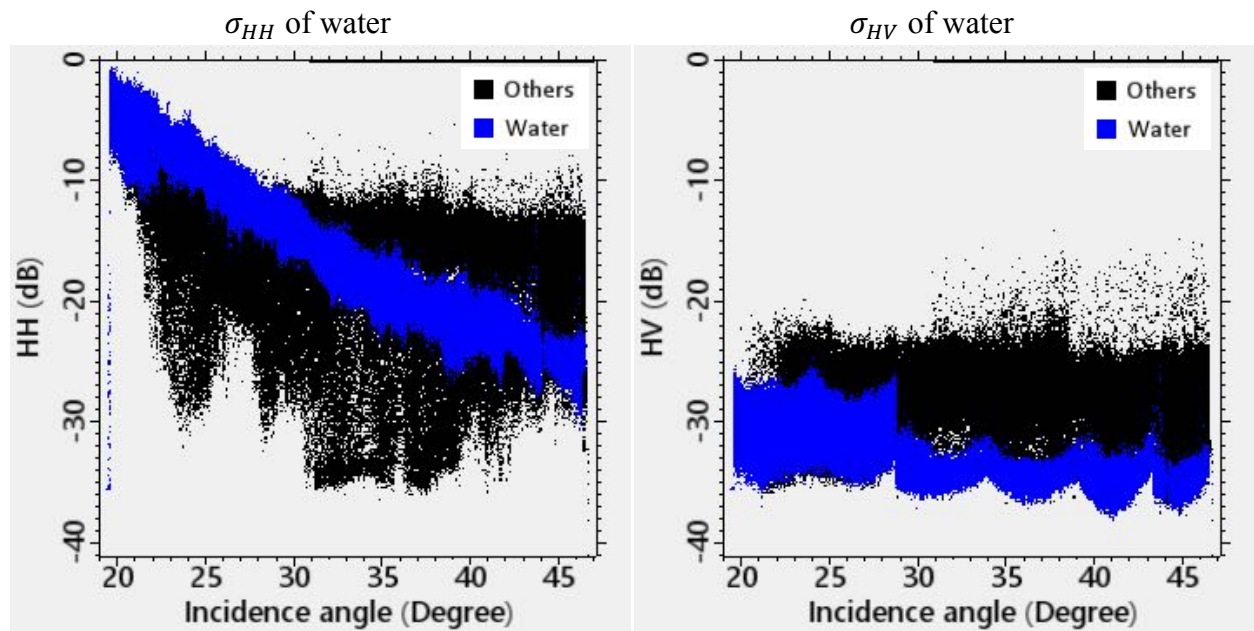
Figure 4.1 Backscatter variation of water in scene captured on January 18, 2016

Figure 4.1 illustrates the backscatter variation on water at different incidence angles in the scene on January 18, where pixels of water were manually selected. σ_{HH} of water has very large variation from around 0 to -30 dB, which may largely affect classification purely from σ_{HH} values. However, an obvious linear trend could be found as incidence angle increase, σ_{HH} of water decrease, which corresponds well with previous literature on ScanSAR imagery.

In terms of σ_{HV}, water shows a "W" shape pattern as incidence angle increase which may be caused by TOPS mode in Sentinel-1, and in the first sub-swath water shows larger variation compared to the rest, but generally σ_{HV} is not obviously affected by incidence angle. A comparison of noise floor in HV of RADARSAT-2 and Sentinel-1 could be found in Appendix B. With this special pattern in HV in Sentinel-1 imagery, previous methods used in ScanSAR images, for instance, IRGS (Yu et al., 2012) which perform initial segmentation on HV bands, may not be applicable. Besides water, no obvious backscatter intensity differences were found in different incidence angles in most sea ice types. In addition, from the σ_{HV} values shown in Figure 4.1, majority of the values were below the noise floor in HV. Though the values would be unreliable, some patterns of ice and water could be found. The special noise pattern in HV in Sentinel-1 imagery is significantly stronger in water compared with ice, such pattern could be considered as a special feature identifying certain classes.

However, despite some patterns could be found in HV, the noise pattern in the first sub-swath brings too many uncertainties as the backscatter values greatly constrains the identification of different ice types and water. In addition, no consensus has been made on the cause of the noise and how to remove or reduce it, so that removing the first sub-swath would be a reasonable choice.

4.1.2 Results of Training Sample Selection

The training samples were selected from four scenes: January 4, January 18, March 16 and April 2, 2016, with reference to sea ice charts provided by the CIS. A total of 11353 pixels were selected, and Table 4.1 shows a summary of training samples in the four scenes and mean values of σ_0.

Table 4.1 Mean values of training samples

	January 4		January 18		March 16		April 2	
	σ_{HH}	σ_{HV}	σ_{HH}	σ_{HV}	σ_{HH}	σ_{HV}	σ_{HH}	σ_{HV}
New ice	-21.1	-33.8	-32.4	-33.9	-23.8	-34.4	NA	NA
Grey ice	-14.2	-27.7	-12.8	-23.5	-16.5	-29.4	-14.7	-29.1
Grey white ice	-9.9	-22.3	-15.6	-28.3	-11.1	-26.7	-13.6	-25.7
Thin first year ice	-10.3	-22.1	-19.9	-33.0	-21.8	-33.8	-10.1	-26.4
Medium first year ice	NA	NA	NA	NA	-10.2	-22.4	-11.6	-23.0
Water	-7.28	-25.7	-18.4	-34.4	-14.0	-33.8	-16.9	-29.1

The unit of σ_0 is dB; NA: not applicable

As shown in Table 4.1 mean σ_{HH} and σ_{HV} values were very different in ice across different scenes and few patterns could be found. The ice types in different scenes are visually different as well only from σ_{HH} and σ_{HV}. Taking grey ice and grey white ice as an example, grey white ice is thicker than grey ice, which may result in higher response in both σ_{HH} and σ_{HV} from literature, but in the scene on January 18, 2016, grey ice has both higher σ_{HH} and σ_{HV} values. In addition, in water class, mean σ_{HH} values are highest among all the classes, except for the scene on April 2, 2016, where water locates at larger incidence. This may be a result of the incidence angle effect on water in σ_{HH}.

Two scatterplots are shown in Figure 4.2 to show the separability of training samples in this scene. From the scatterplot on the left, it can be found that water has a large variation in σ_{HH} and values decrease as incidence angle increase, but other classes are relatively stable. No significant variation in σ_{HV} was found in all classes so that the scatterplot is not shown. From the scatterplot on the right, it can be concluded that water has the largest variation in both σ_{HH} and σ_{HV}, so that it could be mixed with ice classes just from a numerical perspective. New ice also showed some variation in σ_{HH} as some samples were selected in the first sub-swath. Grey ice and grey white ice have very similar σ_{HH} values, but some separability could be found in σ_{HV}. New ice, thin first year ice and water are close in σ_{HH} values, while they could be easily separated in σ_{HV}. However, there are still some confusions majorly from the large variation of backscatter from water.
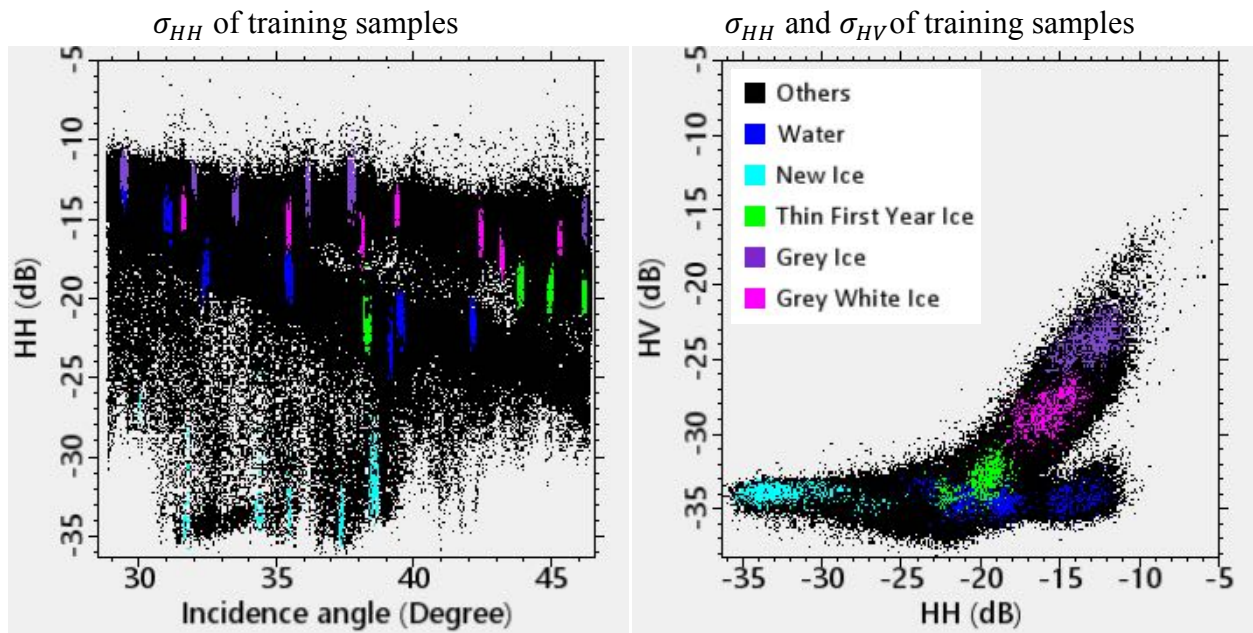
Figure 4.2 Scatterplots of training samples in the scene on January 18, 2016

Considering the noise floor of Sentinel-1 EW mode is -22dB, most of the σ_{HV} values in the images involved in this thesis were below -22dB, making the backscatter from HV unreliable.

However, the differences in σ_{HV} values of different ice types can still be found both visually and from the selected samples shown in Table 4.1 and Figure 4.2. Therefore, HV is expected to have contributions to image segmentation, and feature selection would justify whether HV is effective in identifying ice and water.

4.1.3 Uncertainties and Limitations in Training Sample Selection

All training samples were selected manually based on the author's interpretation of the Sentinel-1 imagery with reference to sea ice charts. However, there are some uncertainties that may lead to errors or deficiency in the training samples.

First, misinterpretation of ice charts may be one of the uncertainties. In ice charts, each polygon marked by egg codes usually contains 2 to 3 classes or even more, which increases the difficulty determining one certain ice type. Figure 4.3 illustrates one scenario of uncertainties in image interpretation, where the image on the left shows part of the ice chart in this region with slight modification and the image on the right is the part of RGB composite of original image in approximately the same region. In Figure 4.3, the triangle shaped area in the middle with the egg code "R" is hard to label from the author's perspective. The egg code "R" suggested the concentration is 3/10, and three ice types: grey ice, grey white ice and new ice, are present, but visually this area has a completely different pattern and color compared to adjacent areas consisting of grey ice and grey white ice. In this case, no training sample were chosen in this area to avoid confusion. In addition, confusion also existed when selecting samples of grey ice and grey white ice. In the region marked with egg code "K", the majority should be grey ice, but this region is obviously brighter than surrounding regions that might be grey-white ice, which is not the case in

50

other scenes. Despite these confusions, samples were selected following egg codes rather than author's experience, but the correctness was not guaranteed.
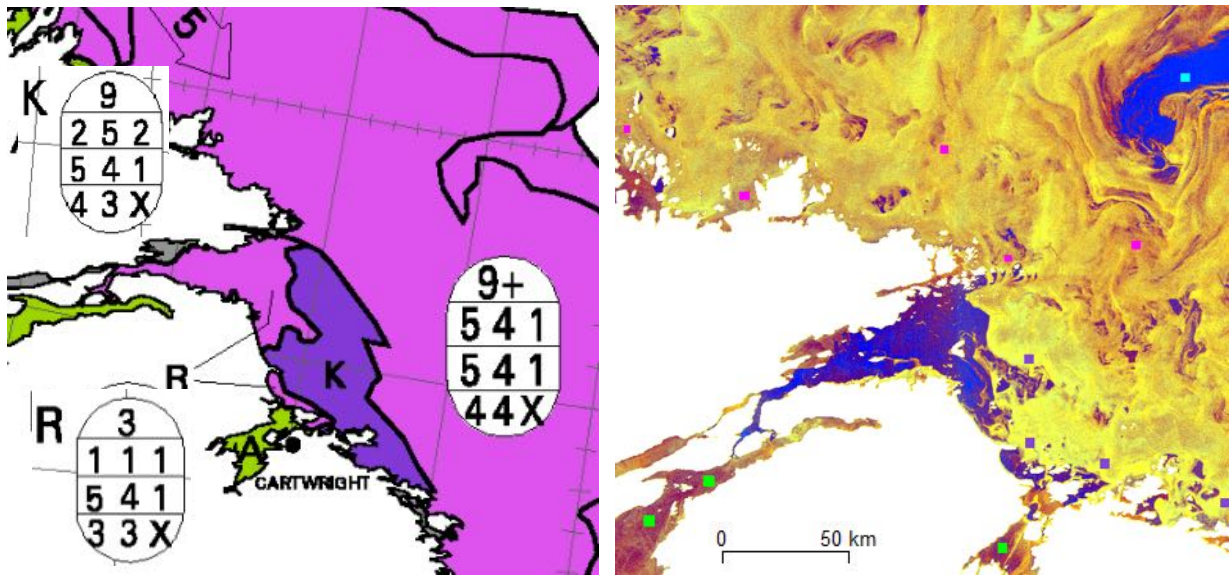
Figure 4.3 Sample of uncertainty in interpreting ice charts in scene on January 18, 2016

Second, the strategy of sample selection may result in uncertainties. In order to efficiently select training samples, the strategy was to select "pure" pixels to capture the most significant features. As a result, some areas with ambiguities such as ice-water boundaries, where several ice types with different flow sizes occur, or where egg codes are difficult to understand, were avoided, and some patterns in these regions may be lost due to complexity and uncertainty.

Finally, the scheme of labels may have an impact on the next steps. During training sample selection, labels were determined by referring to egg codes, and the six classes were: water, new ice, grey ice, grey white ice, thin first year ice and medium first year ice. Among these classes, water itself may have a large variance in σ_0 values. Calm water and wavy water may have very different patterns, while more uncertainties would be added by the incidence angle effect and beam seams. Besides water, thin first year ice may have different responses near the coastline and far

from the coast, since coastal regions may be shallow. Therefore, in an unsupervised classification or segmentation framework, the ideal class scheme may not statistically fit in different images, and sometimes two or more subclasses would be more precise instead of one. However, the training samples were only used in feature selection, and the final segmentation result did not follow the labels in training samples. But a more reasonable class scheme might provide more effective feature selection results.

4.2   Feature Selection

4.2.1   Parameters of Feature Selection

During the three steps in the feature selection algorithm, three corresponding coefficients could be altered to achieve a smaller subset or to improve computational efficiency. Generally, by choosing larger coefficients promotes fewer features and faster selection speed. To determine suitable settings for the three coefficients, an initial run of feature selection using three coefficients as 1 was used as benchmark.

Table 4.2 Twelve most important variables with no parameter settings

Most important variables	Rank	Mean $errOOB$
σ_{HH} Variance 11×11 step 1	1	0.4284
σ_{HV} Contrast 25×25 step 5	2	0.1097
σ_{HV} Mean 11×11 step 1	3	0.0125
σ_{HH} Variance 25×25 step 5	4	0.0035
σ_{HV} Correlation 25×25 step 1	5	0.0016
σ_{HV} Mean 5×5 step 1	6	0.0016
σ_{HV} Dissimilarity 25×25 step 5	7	0.0005
σ_{HH}/σ_{HV} Mean 11×11 step 1	8	0.0002

σ_{HV} Entropy 25×25 step 5	9	0.0001
σ_{HV} Entropy 51×51 step 9	10	<0.0001
σ_{HV} Entropy 51×51 step 5	11	<0.0001
σ_{HH} Mean 25×25 step 1	12	<0.0001

Table 4.2 shows the twelve most important features with no parameter settings, and "Mean $errOOB$" lists the mean $errOOB$s achieved with this feature together with all the features ranked higher. In this run, 131 features were chosen in the thresholding step, 71 features were selected in the interpretation step, and finally 12 features were selected after the prediction step. From Table 4.2, it could be observed that some of the features are the same GLCM features with different window size and step size settings, for example, "σ_{HH} Variance 11×11 step 1" and "σ_{HH} Variance 25×25 step 5", "σ_{HV} Mean 11×11 step 1", "σ_{HV} Mean 5×5 step 1" and "σ_{HH} Mean 25×25 step 1". As these features would have high correlations, the list of 12 selected features may have some redundancy and a smaller set of features could be found with appropriate adjustments of the three coefficients. By conducting tests on how each of the three coefficients affects the number of features selected in each step, suitable coefficients could be selected.

(a)   (b)
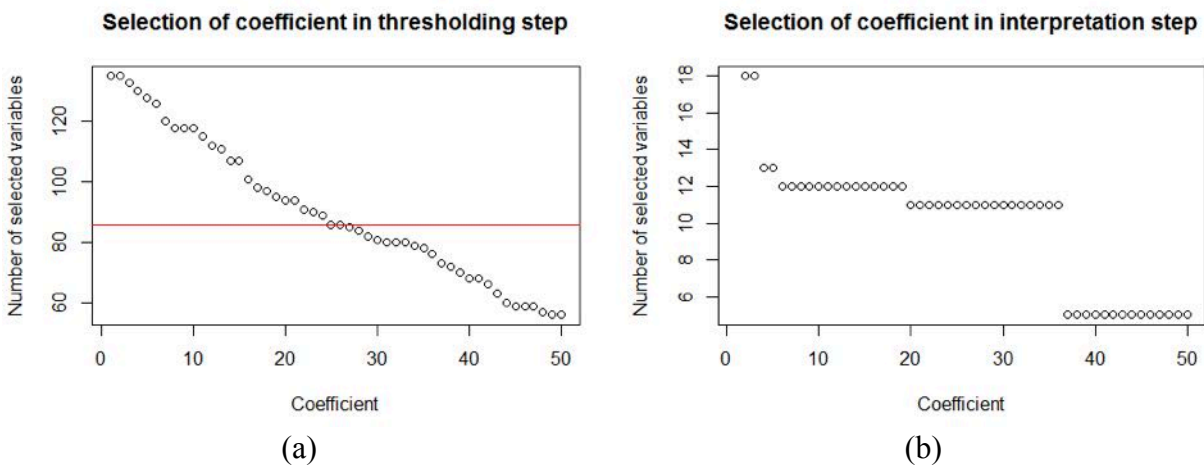
Figure 4.4 Selection of coefficient in feature selection

The first coefficient was used for setting the threshold for feature elimination, and it was multiplied by a minimum variable importance generated by CART function. Fewer features selected in the first step, the faster the interpretation step would be. Figure 4.4(a) shows how coefficient from 1 to 50 would influence the number of selected features in the thresholding step. In this figure, the red horizontal line indicates half of the number of features, 86. The thresholding step aims at removing irrelevant features according to variable importance, thus removing half of the features could be reasonable. Eventually 25 was adopted in the thresholding step, and 86 features were selected.

The second coefficient in the interpretation step determines the smallest number of features that could produce comparable results comparing to which utilizes all features. Figure 4.4(b) illustrates how this coefficient affects the number of feature selected during this step, where two jumps could be found at 11 and 12 variables. The two jumps indicate that the variables rank at 12th and 11th could be able to reduce $errOOB$ significantly. Although another jump would occur when a relatively large coefficient (around 40) was adopted, it would result in only 5 variables selected in this step, which might be too aggressive using this setting. By referring to Table 4.2, the reduction of mean $errOOB$ from the first 12 to 11 features were minimal, and very low error rates could be achieved with 11 features. Thus 20 was selected as the coefficient in the interpretation step, and 11 variables were selected in this step.

In terms of the third coefficient in the prediction step, it determines the final number of most effective features. During the test of this coefficient, 6 features were selected using coefficients from 1 to 30, and a coefficient larger than 30 led to 5 selected features or less. Since a coefficient of 30 would be considerably large, and using 6 features would result in significantly lower mean $errOOB$ compared to 5, no setting of the third coefficient were selected.

4.2.2 Results of Feature Selection

With the three coefficients set as 25, 20,1 respectively, 86 features were selected at the thresholding step, 11 features were selected at interpretation step, and 6 features were finally selected at the prediction step. The final 6 most important features and their mean $errOOB$ achieved with all previous ones are shown in Table 4.3. Among these features, though "σ_{HH} Variance 11×11 step 1" and "σ_{HH} Variance 25×25 step" has a high correlation of more than 0.97, the addition of "σ_{HH} Variance 25×25 step" significantly reduces the error rate, so that it is considered effective.

Table 4.3 Six most important features in the second round

Most important variables	Rank	Mean $errOOB$
σ_{HH} Variance 11×11 step 1	1	0.4285
σ_{HV} Contrast 25×25 step 5	2	0.1099
σ_{HV} Mean 11×11 step 1	3	0.0127
σ_{HV} Correlation 25×25 step 1	4	0.0023
σ_{HH} Variance 25×25 step 5	5	0.0015
σ_{HV} Dissimilarity 25×25 step 5	6	0.0009

Figure 4.5 shows the images of the six selected features in the scene on January 18, 2016. Among the six features, four of them were derived from σ_{HV} and the rest two were from σ_{HH}. The result indicated that HV could make great contribution in separating different ice types and water regardless of its values are below the noise floor. From the appearance of the images of features, features derived from σ_{HH} are still affected by incidence angle on water, while those derived from σ_{HV} have less influence of the banding effect and horizontal lines except "σ_{HV} Mean 11×11 step

1". Therefore, the selected GLCM features from σ_{HV} would mitigate the influence of noise in HV in Sentinel-1 imagery.

σ_{HH} Variance 11×11 step 1	σ_{HV} Contrast 25×25 step 5	σ_{HV} Mean 11×11 step 1

σ_{HV} Correlation 25×25 step 1	σ_{HH} Variance 25×25 step 5	σ_{HV} Dissimilarity 25×25 step 5
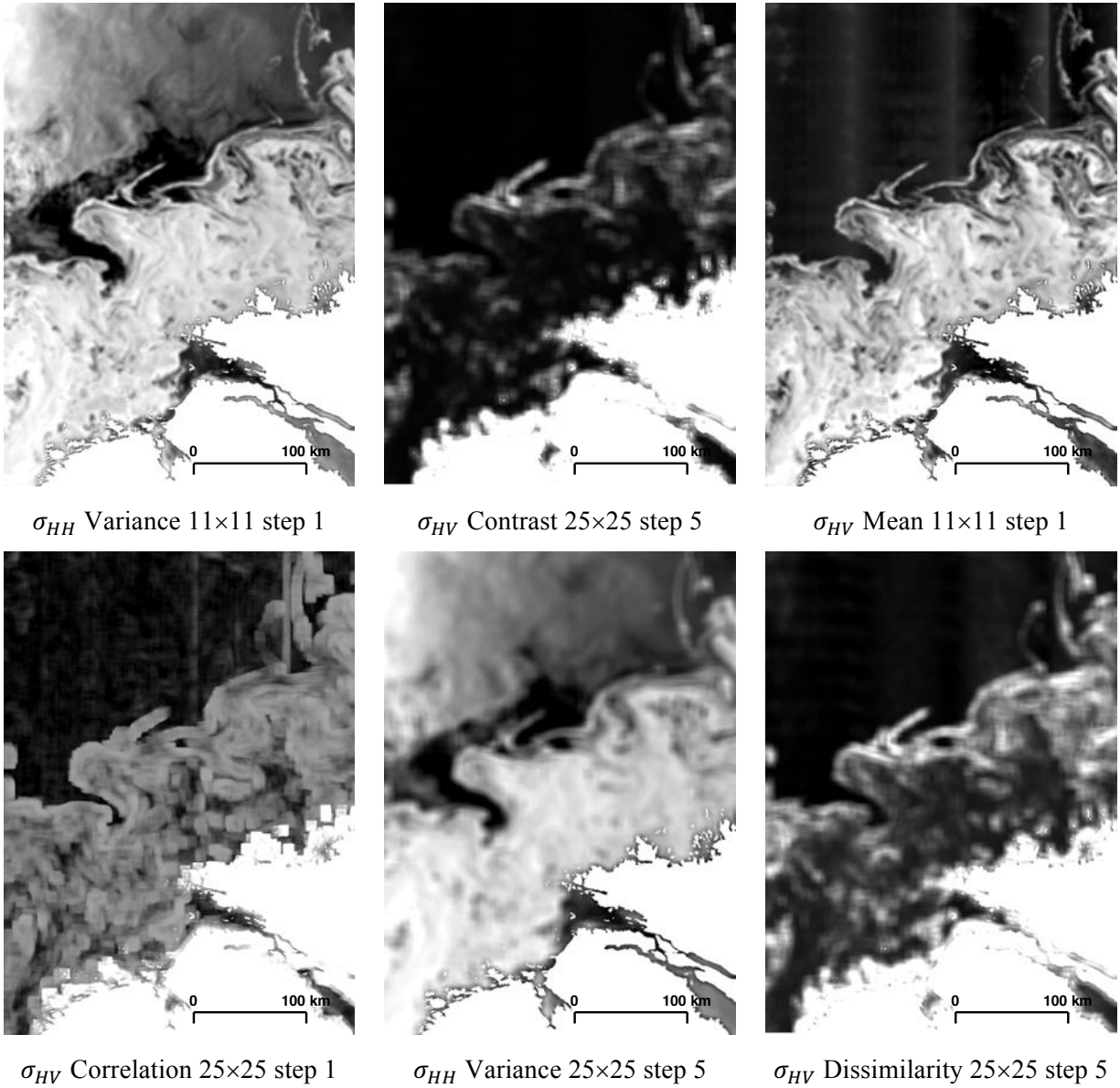
Figure 4.5 Six selected features of the scene on January 18, 2016

4.2.3 Uncertainties and Limitations in Feature Selection

First, the quality of training samples directly affects the results of feature selection. Since the author selected training samples mostly from "pure" pixels and complicated regions were

avoided, uniform characteristics could be expected within each class as well as surrounding pixels. However, some patterns may not be captured due to the strategy, so that these features may not be effective in those complicated regions.

Second, the selected six features from the four scenes may not be the most significant features in each of them. Feature selections were performed in each scene where training samples came from, and Table 4.4 shows the results, in which the window size and step size were abbreviated by: the first number refers to window size and the second number behind underscores represents step size. From the table, the final selected six variables were hardly found, but the same features with different settings could be observed. Therefore, the selected six features may not lead to best performance in distinguishing different ice types and water in a certain scene, but an overall effective differentiation could be achieved.

Table 4.4 Feature selection results of each scene

Rank	0104	0118	0316	0402
1	σ_{HV} Mean 5_1	σ_{HV} Var 25_1	σ_{HV} Mean 11_1	σ_{HV} Mean 11_1
2	σ_{HV} Var 5_1	σ_{HV} SEM 25_5	σ_{HV} Var 11_1	σ_{HV} Mean 25_1
3	σ_{HV} Mean 11_1	σ_{HV} Hom 25_5	σ_{HV} Mean 5_1	σ_{HV} Var 25_5
4	σ_{HV} Var 11_1	σ_{HV} Mean 5_1	σ_{HH} Var 11_1	σ_{HV} Mean 5_1
5	σ_{HV} Hom 51_5	σ_{HV} Mean 25_1	σ_{HH} Mean 11_1	σ_{HV} Var 11_1
6	R SEM 51_5	σ_{HV} Var 5_1	R SEM 25_5	σ_{HH} Hom 25_1
7	R SEM 51_9	σ_{HV} Mean 25_5		R Con 51_5
8	R Hom 51_5	σ_{HH} Var 5_1		R Hom 51_9

Var: Variance; Dis: Dissimilarity; Ent: Entropy; Con: Contrast; SEM: Second moment; Hom: Homogeneity; R: σ_{HH}/σ_{HV} Ratio

Third, the feature selection algorithm itself may not generate the optimal set of variables. In this forward searching algorithm, the searching order is based on the rank of importance produced by random forests. However, most significant individual variables may not eventually transform into an optimal variable set. Though the final 6 variables were able to produce a low error rate, they might not be the most effective set of 6, or a smaller set may exist with comparable performance. Since the data model used in image segmentation was different from random forest, a different variable set might lead to a different result.

4.3   Image Segmentation

4.3.1   Selection of Candidate Parameters

There are three main parameters in the segmentation algorithm in this study: 1) initial number of classes K, 2) w_s as the weight of smooth cost, represented by "scale", and 3) w_l as the weight of label cost. In determination of candidate parameters for final segmentation, the four scenes where training samples were selected form were used as benchmark.

K determines the maximum number of classes during the segmentation process, and tests starting with different Ks were conducted. Generally, the final number of classes is determined by the selection of label cost, and similar results were achieved with different Ks. Thus, K should be set according to a desired final number of classes. In this thesis, only the separation of ice and water would be assessed, so that the optimal final classes would be as water, ice and land. To successfully separate ice and water, 6 classes were used for initial segmentation in IRGS to fit different conditions (Leigh et al., 2014). Therefore, the final number of classes in this thesis would target at around 6 or a smaller number. Finally, 10 was chosen for K at initial K-means labelling to assure completeness of class scheme, and to validate the performance of label cost.

58

The second parameter, scale, determines the smoothness of the segments. With a larger scale, the results would become smooth but some details might not be preserved, while with a small scale, small fragments would remain which affects interpretation. Generally, scale affects the results more from a visual perspective, and a larger scale would promote the merge of classes during iteration. By visual comparison, scale was set to 20 to achieve a sensible smoothness of segments.

The third parameter, label cost, is the most important parameter in this study, which determines how aggressively number of labels are reduced. Generally, a larger label cost promotes smaller number of labels, but may inappropriately merge different classes if the cost is too large. In addition, depending on the distribution of pixel values in different scenes, the same label cost setting may result in different number of labels during image segmentation. Figure 4.6 illustrates the results of label cost testing, and 15, 20 and 25 were chosen since changes in number of labels were observed when scale was 0. Since the target of number of labels may be close to 6 from literature, 6 was considered a benchmark for label cost selection. In the scene on January 4, 2016, class number reduced to 6 at label cost 15, and it reduced to 5 when label cost reached 20 but not further reduced at 25. The scene on January 18, 2016, showed the same pattern. In the scene on March 16, 2016, class number reduced when label cost changed from 20 to 25, and the scene on April 2, 2016 showed the same pattern. After all, the test results indicated that probably no single setting of label cost would fit all scenes, so that these three values should be compared to make a final decision.
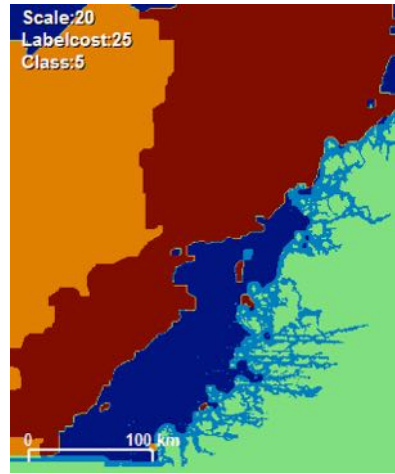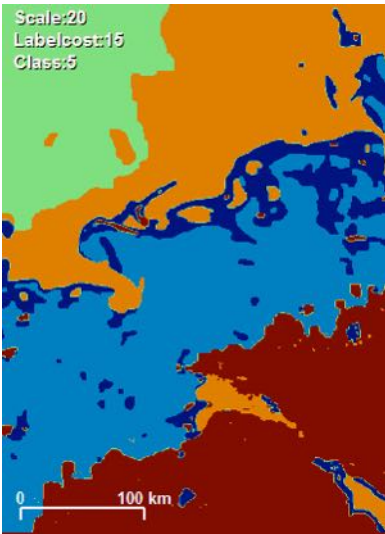
Left: Label cost 15   Middle: Label cost 20   Right: Label cost 25
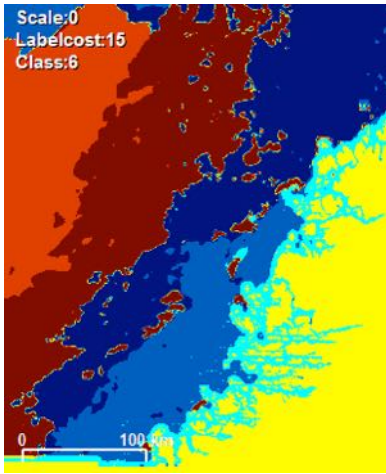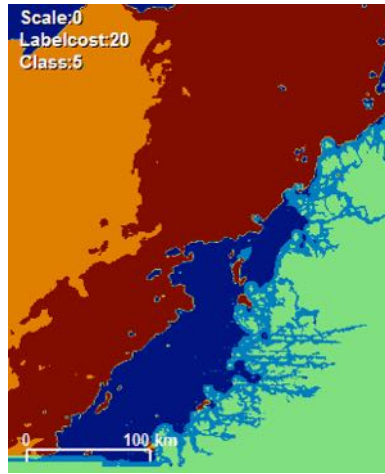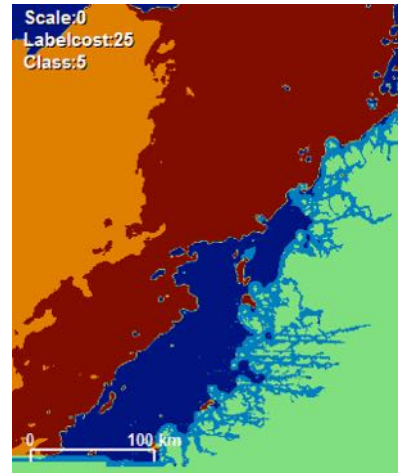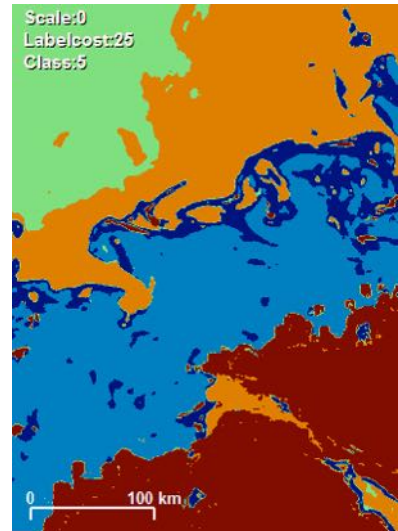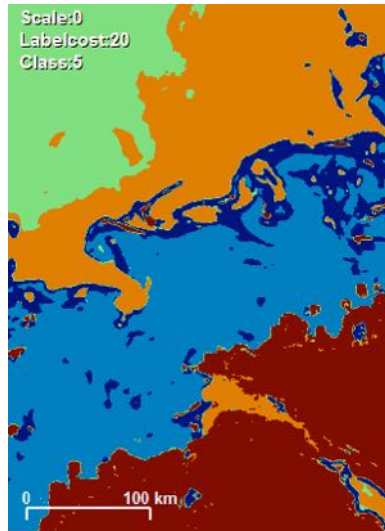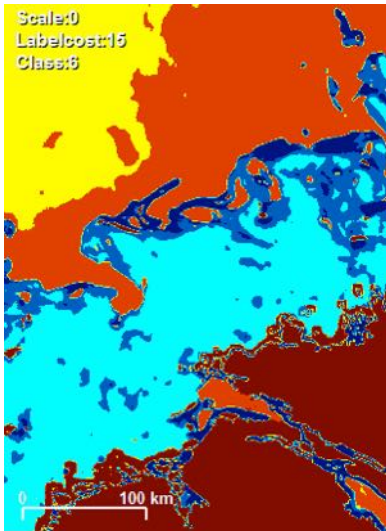

Test of scene on January 4, 2016

Test of scene on January 18, 2016
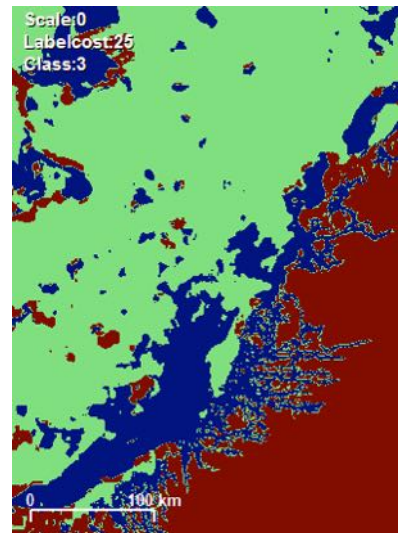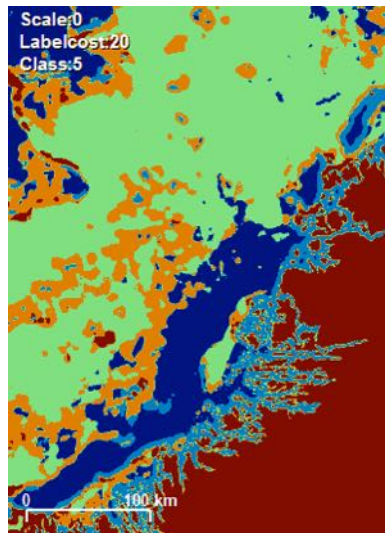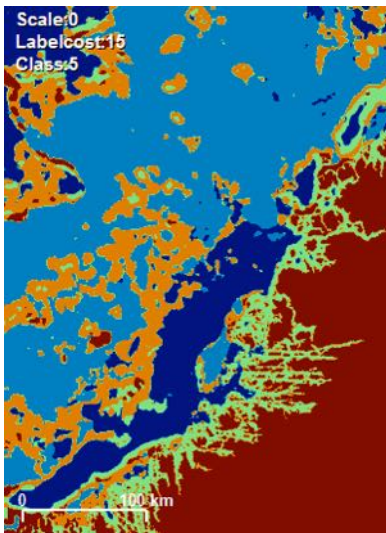
Test of scene on March 16, 2016
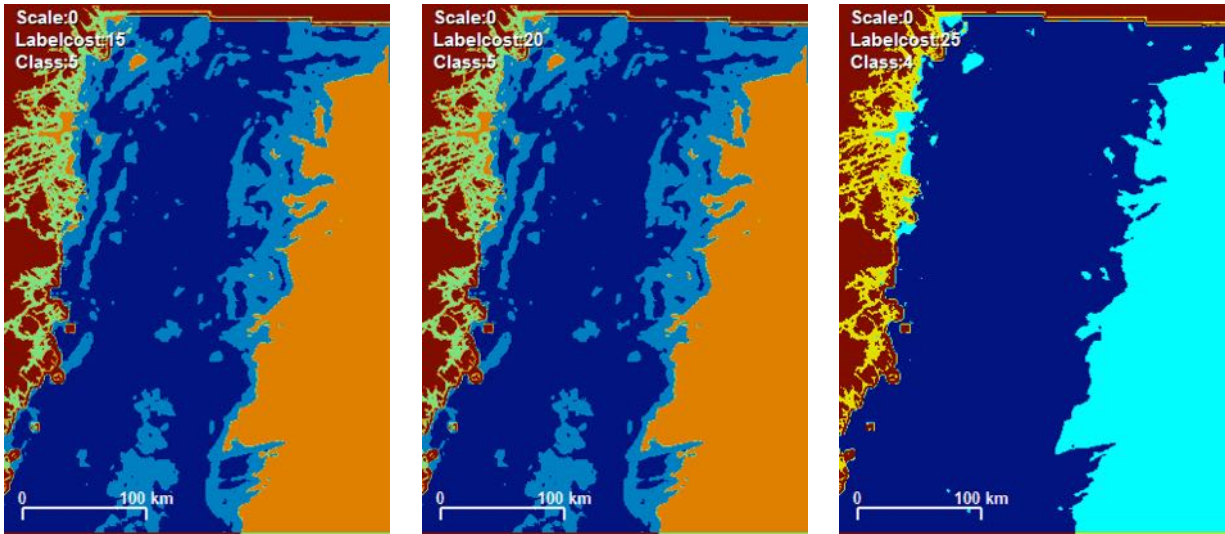
Test of scene on April 2, 2016

Figure 4.6 Results of label cost on test scenes

Therefore, scale of 20, and label cost of three settings, 15, 20 and 25 were considered candidates of parameters, and a preliminary test on these combinations were also conducted on these four scenes. The results are shown in Figure 4.7. The results show that generally the change of number of labels follows the test of label cost in scenes on January 18 and March 16, 2016, but the larger scale promotes reduction of labels earlier in the other two. Thus the choice of candidate parameters is reasonable. The three label cost settings were carried on to all 15 scenes, and an accuracy assessment was conducted to evaluate the performance on water identification. However, the scenes on December 28, 2015 and February 14, 2016 does not contain water after the removal of the first sub-swath, they could not be evaluated on identification of water. As a result, only 13 images were evaluated.

Left: Label cost 15   Middle: Label cost 20   Right: Label cost 25
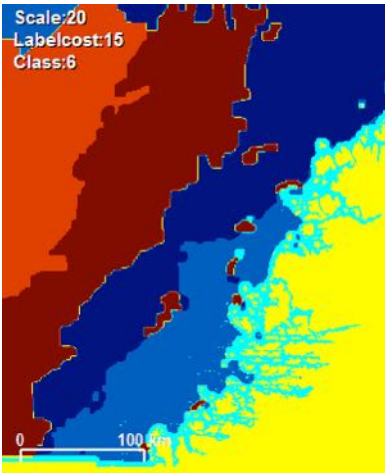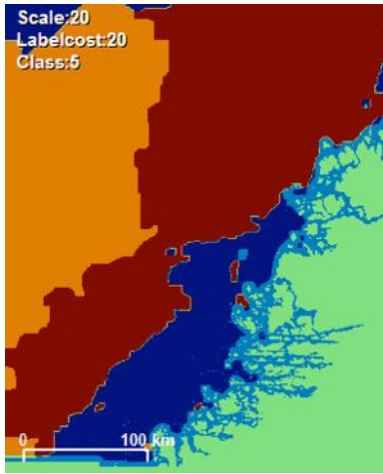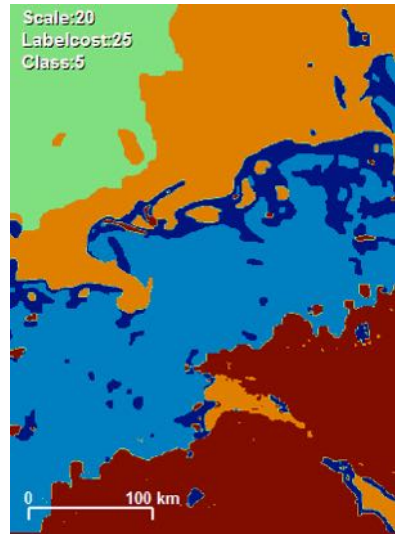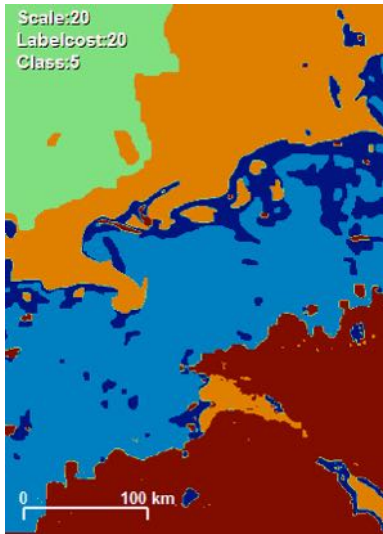
Test of scene on January 4, 2016

Test of scene on January 18, 2016
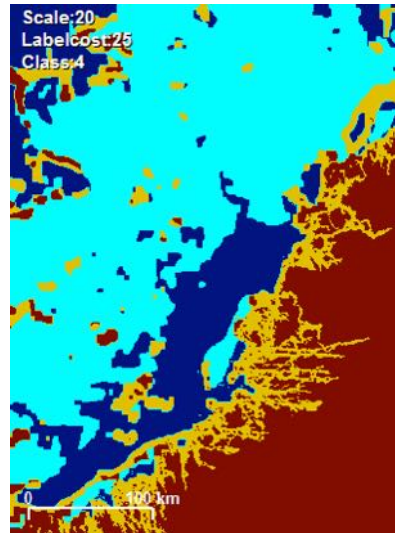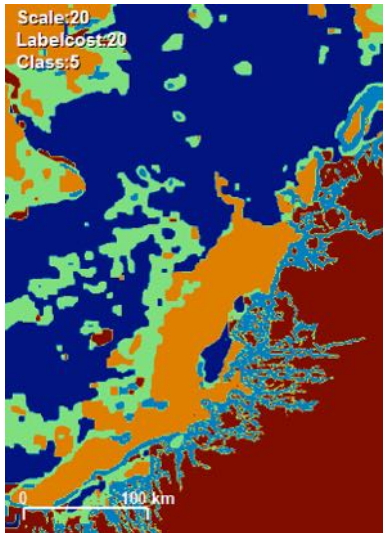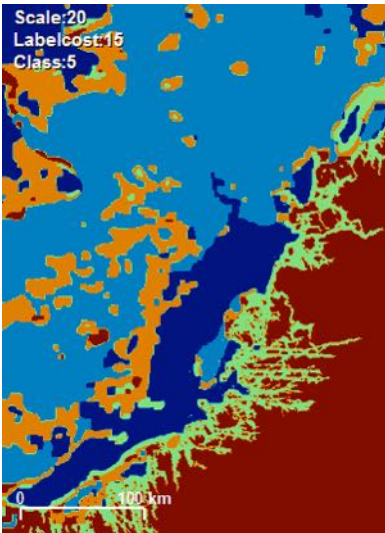
Test of scene on March 16, 2016
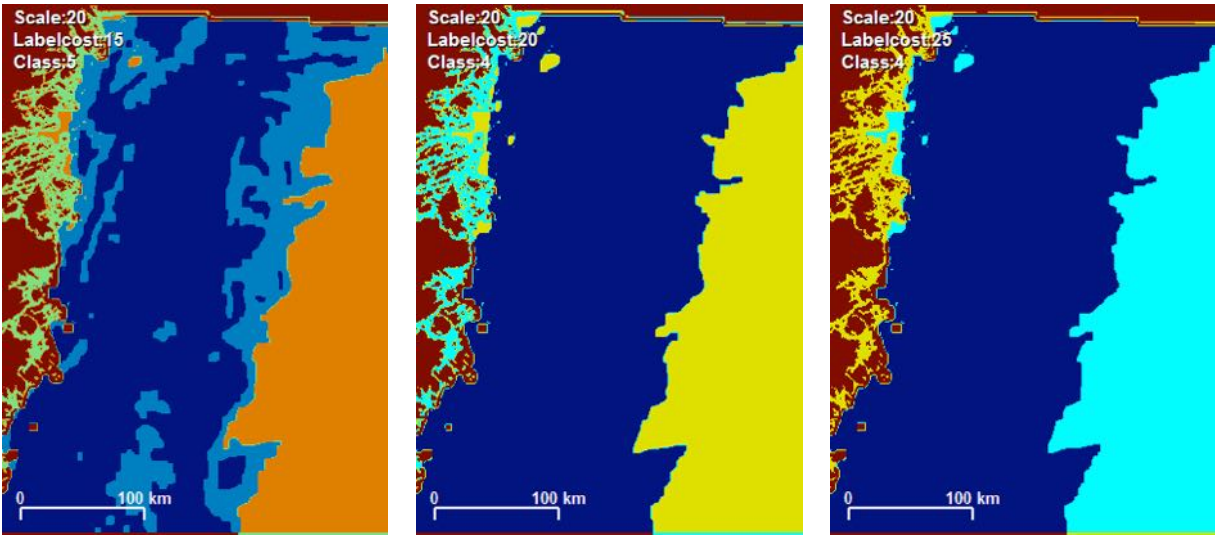
Test of scene on April 2, 2016

Figure 4.7 Results of candidate parameters on test scenes

4.3.2 Results of Image Segmentation

The results of accuracy assessment using the three label cost settings are listed in Table 4.5. Generally, all three settings generated sensible results in distinguishing water from other classes, with the overall accuracy of 94.9%, 92.4% and 91.9%, respectively with label cost settings as 15, 20 and 25, respectively. With the increase of label cost, number of total labels and number of water labels decrease, which may be the cause of overall accuracy decrease as some classes were unnecessarily merged during optimization. By comparing the producer's accuracy and the user's accuracy, it can be observed that producer's accuracy is higher than user's accuracy in all three cases, which means that certain types of sea ice may have very similar response to water. However, the producer's accuracies could reach over 96% percent, indicating that most of the water in the images could be identified.

Table 4.5 Accuracy of image segmentation

Date	Label cost 15					Label cost 20					Label cost 25				
	UA	PA	OA	NT	NW	UA	PA	OA	NT	NW	UA	PA	OA	NT	NW
0104	75.4%	83.6%	94.7%	6	1	47.5%	85.6%	86.8%	5	1	47.5%	85.6%	86.8%	5	1
0111	90.1%	96.6%	96.0%	7	2	90.1%	96.6%	96.1%	7	2	91.8%	96.1%	96.5%	4	1
0118	61.8%	99.8%	85.4%	5	2	61.6%	99.8%	85.3%	5	2	61.9%	99.8%	85.5%	5	2
0121	85.3%	91.2%	97.9%	4	1	29.3%	99.9%	79.5%	3	1	29.3%	99.9%	79.5%	3	1
0204	88.3%	99.4%	96.0%	6	2	87.9%	99.3%	95.9%	5	2	88.0%	99.3%	95.9%	5	2
0316	14.2%	88.2%	86.9%	5	1	14.2%	88.8%	86.7%	5	1	12.4%	89.9%	84.5%	4	1
0323	95.3%	95.9%	97.0%	8	3	96.2%	95.2%	97.0%	7	2	85.9%	98.1%	93.8%	4	2
0402	97.6%	86.9%	95.8%	5	1	93.4%	91.1%	95.8%	4	1	93.4%	91.1%	95.8%	4	1
0409	96.7%	98.7%	97.4%	4	1	96.7%	98.7%	97.4%	4	1	96.7%	98.7%	97.4%	4	1
0426	88.7%	84.2%	95.2%	5	1	87.8%	84.2%	95.1%	4	1	78.3%	86.4%	93.3%	3	1
0520	90.9%	99.6%	95.4%	4	1	86.5%	99.9%	93.1%	3	1	86.5%	99.9%	93.1%	3	1
0527	97.1%	98.6%	97.0%	5	2	93.0%	99.0%	94.1%	4	2	93.0%	99.0%	94.1%	4	2
0613	97.8%	99.5%	98.3%	3	1	97.8%	99.5%	98.3%	3	1	97.8%	99.5%	98.3%	3	1
Overall	88.4%	96.6%	94.9%			82.4%	97.2%	92.4%			81.2%	97.5%	91.9%		

PA: producer's accuracy; UA: user's accuracy; OA: overall accuracy; NT: number of total labels; NW: number of water labels

Shaded areas shows the results using finally selected parameter setting

By comparing the three label cost settings, 15 generated the highest user's accuracy and overall accuracy. The label cost of 20 led to slightly higher producer's accuracy but lower user's accuracy, while reduced number of labels could be observed. The label cost setting of 25 further reduced the number of labels, and the user's accuracy and producer's accuracy also decreased, but the producer's accuracy slightly increased. The larger label cost settings may result in excessive merging of some classes so that producer's accuracy increases at the cost of user's accuracy.

All the segmentation results are listed in Appendix C, together with RGB combination of the original Sentinel-1 imagery and ground truth.

4.3.3   Discussion of Specific Scenes

From Table 4.5, it can be observed that most of the scenes were well-segmented. Some scenes that are worth noting are discussed as follow.

4.3.3.1   *Ideal Segmentation: Result of Scene on June 13, 2016*

(a) Segmentation result   (b) RGB image of data   (c) Reference map of water
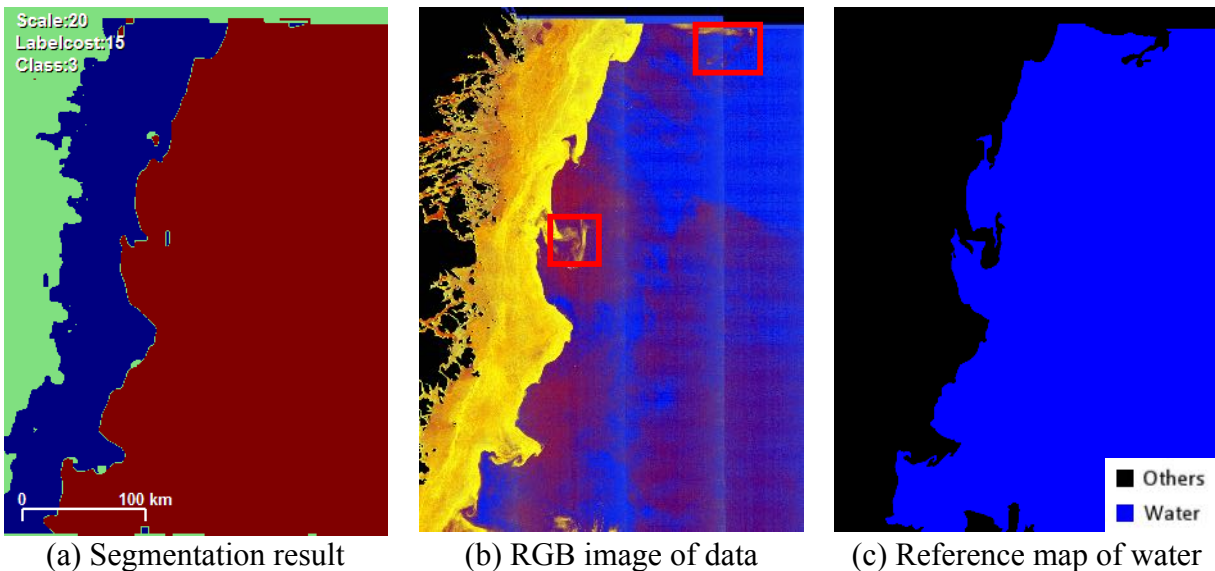
Figure 4.8 Segmentation result of scene on June 13, 2016

Figure 4.8 shows the results of scene on June 13, 2016, which could be considered as an ideal segmentation result in terms of water identification as only three classes: sea ice, water and land could be identified, and the user's accuracy, the producer's accuracy and the overall accuracy reached 97.8%, 99.5% and 98.3% respectively.

The algorithm was able to identify majority of water in this scene, except for some small areas that may be relatively thin ice, as shown in the two red squared boxes in Figure 4.8(b). These areas might be ambiguous to identify at the ice-water boundary, so that the misidentification would be acceptable.

In the water class, some areas that may be covered by very thin ice spreading in the water area was successfully identified and merged with the water class. In addition, one vertical line which is the beam seam at the right part of the image was not affecting the segmentation result. The successful segmentation result indicated that the selected six features were able to capture significant patterns of water and ice, and some influences of noise could be mitigated.

4.3.3.2 *Lowest User's Accuracy: Result of Scene on March 16, 2016*

The segmentation result of scene on March 16, 2016 is shown in Figure 4.9, and the result achieved the user's accuracy of 14.2%, which is the lowest among all the results of 13 scenes. In addition, with the other two candidate label cost settings: 20 and 25, the user's accuracy did not increase. But the producer's accuracy reached 88.2%, which is below average but still could be considered good.

By comparing Figure 4.9(a) and Figure 4.9(b), which are the segmentation result and the RGB image, it could be found that the ice type in the red box was considered the same type with water. According to the ice chart on that date, the marked ice type was majorly new ice, which is

the type that is difficult to separate from water. Though the water identification was not successful, the segmentation of water and new ice in this scene were relatively complete and accurate by visual comparison with the ice chart. Further tests on using different label cost settings did not provide satisfying results so that the mislabelling could be owed to the backscatter similarity between new ice and water. Therefore, the result shows that the discrimination between new ice and water needs to improve to achieve an accurate segmentation result.

(a) Segmentation result   (b) RGB image of data   (c) Reference map of water
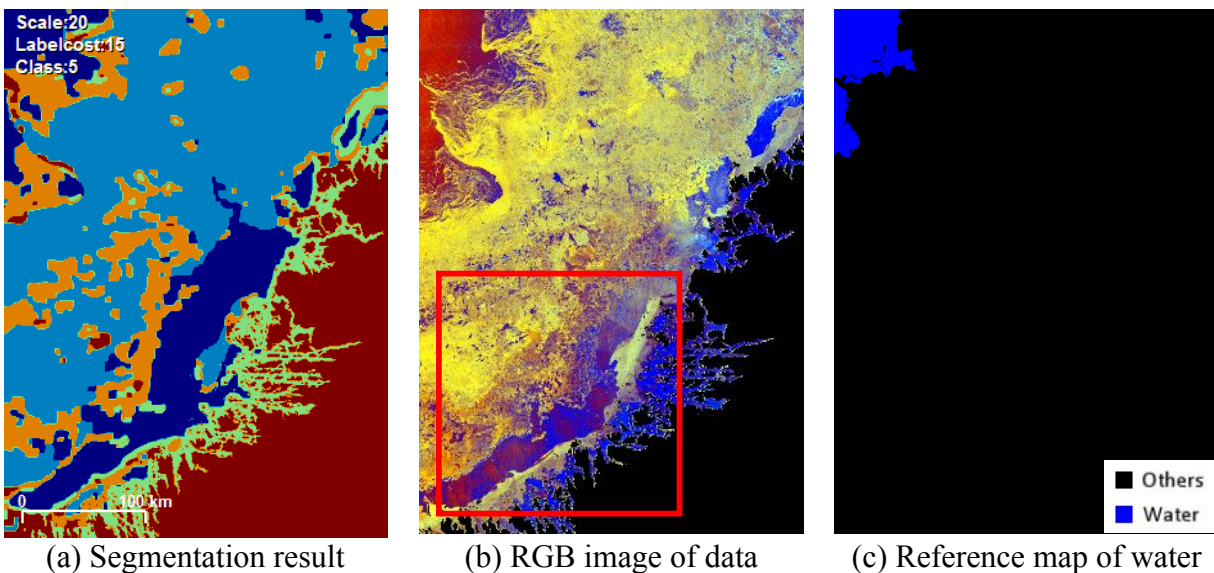
Figure 4.9 Segmentation result of scene on March 16, 2016

4.3.3.3 Most Number of Labels: Results of Scene on March 23, 2016

Among the segmentation results achieved using label cost of 15, the results of scene on March 23, 2016 resulted in the most number of labels. As Figure 4.10(a) shows, a total of 8 labels were produced by this segmentation algorithm, and 3 of them were presenting water. Both numbers are the highest among all the segmentation results listed in Table 4.5. Though the large number of labels makes image interpretation unintuitive, user's accuracy, producer's accuracy and overall

accuracy reached 95.3%, 95.9% and 97.0% respectively, which could be considered a successful segmentation result.

(a) Segmentation result   (b) RGB image of data   (c) Result with label cost 25
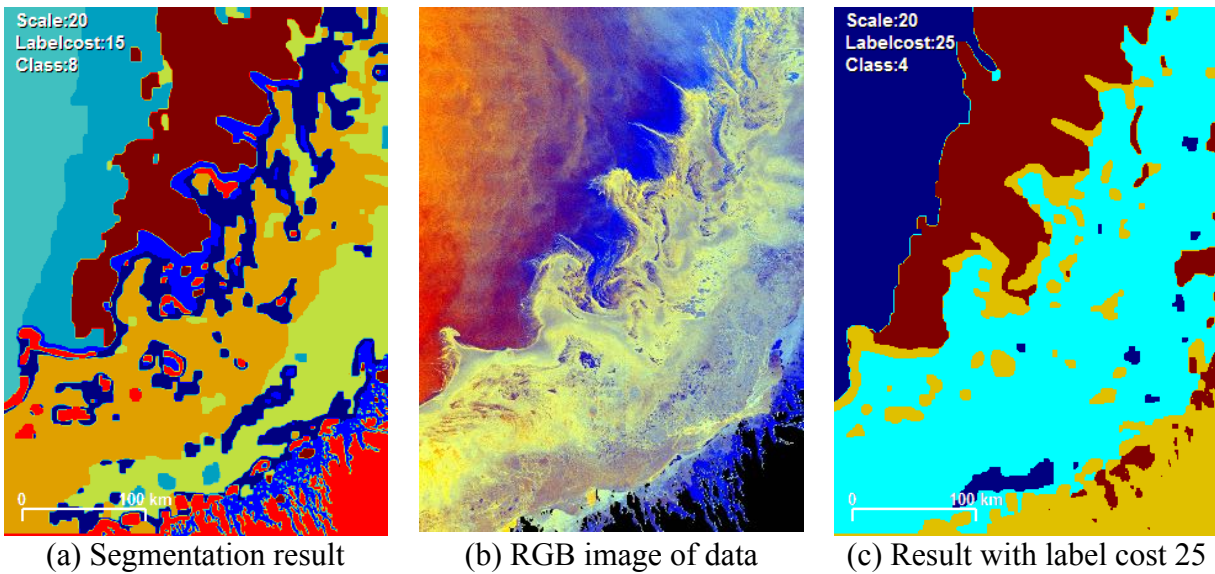
Figure 4.10 Segmentation results of scene on March 23, 2016

However, a better segmentation result could be achieved as the number of labels has the potential to be further reduced. By referring to the results shown in Table 4.5, the number of class reduces as label cost increases to 20 and 25. As shown in Figure 4.10(c), with the label cost setting at 25, 4 total number of labels were produced by the segmentation algorithm, among which 2 classes represents water, but by further increasing label cost, unreasonable results were produced because of excessive merging. The label cost setting at 25 resulted in user's accuracy, producer's accuracy and overall accuracy of 85.9%, 98.1% and 93.8% respectively. The larger label cost resulted in 10% decrease in user's accuracy since some ice areas were incorrectly merged with water at the right side of the image as shown in Figure 4.10(c), but the reduction in overall accuracy was not that obvious. Therefore, though lower user's accuracy were generated with the large label cost setting, 25 may be considered a better choice in the scene on March 23, 2016 since it reduces

68

number of labels significantly, enabling more intuitive interpretation of water contents in the image in the scope of the study.

In addition to this scene, the scenes on January 11, February 4, April 2, April 26, May 20 and May 27, 2016 could also result in smaller number of labels with a larger label cost setting without sacrificing accuracy significantly. Therefore, the label cost setting of 15 does not necessarily provide best performance in all scenes, and better results could be provided in terms of ice-water identification, but 15 resulted in an overall best performance.

4.3.3.4   Uncertainties of Some Ice Types: Results of Scene on January 18, 2016

(a) Segmentation result   (b) RGB image of data   (c) Reference map of water
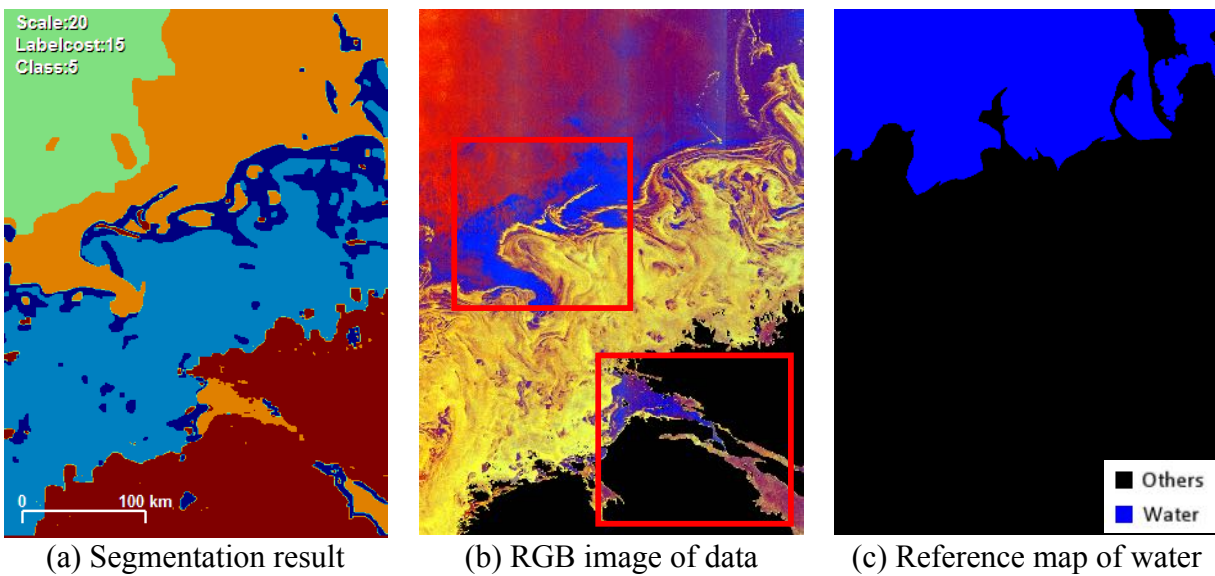
Figure 4.11 Segmentation result of scene on January 18, 2016

Figure 4.11 illustrates the segmentation result of the scene on January 18, 2016, the user's accuracy, producer's accuracy and overall accuracy were 61.8%, 99.8% and 85.4%, respectively. The relatively low accuracy was mainly caused by the mislabelling in the two areas in red boxes as shown in Figure 4.11(b). In the upper red box shows an area that might be new ice, as evidence could be seen in HH but not in HV (as shown previously in Figure 3.3). This region was labeled

as ice in manual labelling and training sample selection, but it is questionable as the backscatters were below the noise floor in both σ_{HH} and σ_{HV}. Another area shown in the lower red box shows the area close to the land, and the area would be ambiguous as low concentration of ice were found in the ice chart. The regions close to land may have more uncertainties as the radar backscatters may be influenced by water depth below ice or the regions could be ice frozen to the ground. The selected six features were not able to successfully capture effective patterns to distinguish water and ice, and the algorithm could be further improved in these ambiguous regions.

4.3.4   Uncertainties and Limitations in Image Segmentation

The results of the selected parameter setting could generate results of close to 95% in the overall accuracy. However, there are some identified uncertainties and limitations in the image segmentation process.

First of all, according to the results listed in Table 4.5 and the discussions on specific images, it could be concluded that no parameter setting was perfect for all of the 15 images, or even most of them, not mentioning if the method is applied in operational image segmentation. In evaluation of successfulness of water identification, the appropriate number of labels might vary. Even though the label cost settings could decrease the number of labels in each image, different data distribution, different ice types and different incidence angles may result in different number of labels during the optimization process. For each specific image, the optimal parameter set may be found and better labelling result could be achieved, but one setting that fits all scenes was not guaranteed. After all, the "best" parameter set was limited on the performance of the 13 selected images in this study, but when the method is applied in other images, the best setting may be different.

Second, in this study, the selected features and the data model may not be optimal. As discussed in Section 4.2.2, the banding effect of Sentinel-1 imagery were mitigated by the selected features to some extent, but some parts of water may be similar to some ice classes in some cases. That might be the trade-off of solving one specific problem. In addition, the features were selected using random forests, which are based on decision trees with arbitrary thresholds, but the data model used in segmentation optimization was not. Consequently, high classification results in features selection may not necessarily lead to satisfying labelling results. Most importantly, only the GLCM features with limited variations were selected, other spatial features could be effective as well. In terms of selection of data model, Euclidian distance was chosen, but it may not work well with the selected features or the Sentinel-1 SAR imagery.

Third, short of ground truth may result in biased training sample selection and accuracy assessment. As discussed in Section 4.2.3, training sample selection based on the author's preferences may not have a complete representation of each class. In addition, the misinterpretation of ice chart could bring error and uncertainties in the selected samples. This kind of problem also exist when manually providing ground truth for water, especially at ice-water boundary. The boundaries of water and ice are very smooth in ice charts, while the true boundaries are not. Since very thin ice may not be captured by C-band SAR imagery, these "ice-water" boundaries in this thesis could actually be the threshold of whether ice could be identified by the sensor. Considering the development or melting of ice is a gradual process, the threshold might not be easy to find.

4.4   Chapter Summary

This chapter displayed the detailed results of each step of the proposed workflow, including training sample selection, features selection and image segmentation. The uncertainties and

71

limitations in each step were discussed. The segmentation results of 13 testing Sentinel-1 SAR images were evaluated using an error matrix. The overall accuracy reached close to 95%, and the final segmentation maps are displayed in Appendix C.

Chapter 5   Conclusions and Recommendations

5.1   Conclusions

Sea ice monitoring is crucial to several invaluable purposes, including study of climate, marine navigation and coastal resource development, especially for coastal regions, such as Labrador coast. SAR imaging satellites has been approved as an important data source for sea ice monitoring in Canada. However, the limited revisiting time of a single SAR satellite such as RADARSAT-2 and large volume of manual work are two main challenges in providing high-quality sea ice map products timely and effectively. To deal with the two challenges, new data sources and automated image processing algorithms are in demand. This thesis proposed a prototype semi-automated SAR image segmentation workflow, which has been tested on 15 scenes of Sentinel-1 SAR images in the study area of Labrador coast.

There are three main objectives in this thesis, 1) to determine the most important features in identifying different types of sea ice, 2) to examine the effectiveness of the proposed workflow, and 3) to evaluate the capability of Sentinel-1 SAR imagery in sea ice mapping. In order to address these objectives, the methodology was designed by three main components: 1) The GLCM features were calculated in various window sizes and step sizes, and a variable selection algorithm based on random forests were used in determining the most important features; 2) A segmentation optimization algorithm based on graph cut was deployed with the integration of label cost, and the images could be segmented into different numbers of labels with different settings; and 3) An accuracy assessment was conducted to evaluate how well the segmentation results in identifying water contents in Sentinel-1 imagery. This thesis did an exploration on a prototype automated image segmentation method, and experimental results derived some insights on the three objectives. The results are concluded as follow.

73

First, six GLCM features were selected as the most significant features in distinguishing water and different ice types. These six features are: σ_{HH} Variance 11×11 step 1, σ_{HV} Contrast 25×25 step 5, σ_{HV} Mean 11×11 step 1, σ_{HV} Correlation 25×25 step 1, σ_{HH} Variance 25×25 step 5, and σ_{HV} Dissimilarity 25×25 step 5. Second, the proposed method was able to segment the 13 test images into 3-8 classes with the selected parameter set, which may potentially provide a solution to determining the optimal number of labels. However, it was also found that one setting of parameters was not able to provide optimal results in all images. Third, in Sentinel-1 SAR imagery, incidence angle effects in co-polarized bands of water and banding effects in cross-polarized bands may affect the interpretation of sea ice, but these effects were mitigated by the selected features and the segmentation algorithm. The overall accuracy of the tests reached 95% in distinguishing water in the images, and most errors comes from the similarity between water and thin ice types. After all, higher accuracies could be achieved when tuning parameters in individual images, but it may not be applicable if an automated method is needed.

In conclusion, Sentinel-1 SAR imagery is able to monitor sea ice conditions successfully, and the proposed workflow has the potential of developing into an automated image segmentation solution.

5.2   Recommendations for Future Work

The uncertainties and limitations of the study have been discussed in Chapter 4, and more work and experiments could be done in the future to improve the performance of the proposed method.

Firstly, ground truth with higher quality would be an urgent need for the improvement of the method. In this thesis, training samples and validation samples were manually selected by the

author while misinterpretation and uncertainties may result in deficiencies of the workflow. With more precise ice labelling, the selected features would be more representative and efficient. Additionally, with better ground truth, the effectiveness of ice type segmentation using this proposed method could be validated as well, but more labels are needed and the parameter settings would be different.

Secondly, more texture features need to be tested and evaluated. In this thesis, only GLCM was calculated with limited settings, while a different setting for GLCM (Clausi, 2002) or more features such as Gabor filter, MRF features (Clausi, 2001) should be tested.

Thirdly, different data models could be used in the segmentation optimization process. In this thesis, the basic Euclidian distance was adopted, while the problem of singularity prevented a comparison test using Gaussian model or other data cost models limited to the author's knowledge and time. The solution to this problem should be found, better results could be achieved.

Fourthly, a better use of Sentinel-1 imagery could be helpful. In this thesis, down sampled Sentinel-1 GRDM images were used in testing the methodology. However, tests could be done at a higher resolution. Since Sentinel-1 imagery can be accessed free of charge, more images and different products could be tested as well. In addition, only magnitude was used in this thesis, phase information could also be helpful, and new features could be explored. Temporal information could also be an asset, as the short revisiting time of Sentinel-1 could be taken advantage of.

Fifthly, some ancillary data could be combined for better sea ice identification. Image fusion with images from other sensors has been demonstrated successful in sea ice image interpretation (Wang et al., 2016; Casey et al., 2016), and meteorological data might help determine development stage of ice and ice conditions.

Sixthly, the noise pattern of Sentinel-1 needs to be further studied, especially in cross polarization. In this thesis, the first sub-swath, where largest affected by noise, was removed to achieve better interpretation of the images. However, the first sub-swath still contains reasonable information about ice and water, which would be explored. Some effective features would exist to effectively identify ice types and water even if this sub-swath is kept, systematic noise reduction methods such as some frequency filters should be tested on whether this noise could be reduced. In addition, the results of this study indicated that though most backscatter values of HV are below the noise floor, HV contributed significantly in the segmentation. The effective values of backscatters in HV should be further explored to make better use of Sentinel-1 imagery. As the noise floor of the RCM is also -22dB, the same problem would exist in the RCM imagery, thus the exploration of HV values below noise floor would provide valuable references when processing the RCM products.

Finally, although the proposed method was able to generate good results and improvements could be made, the author still believes that deep learning methods are the future in sea ice analysis, and experiments (Wang et al., 2016) has demonstrated the power of deep learning. Traditional methods, such as the one presented in this thesis, might only able to study limited aspects of sea ice SAR imagery, and the hierarchical learning capabilities of deep learning methods may generate more promising results. Deep learning methods might be limited due to lack of training sets, but with the free of charge Sentinel-1 imagery, building a large enough image library of sea ice might be feasible.

References

Alaska Satellite Facility, 2016. *Sentinel image quality*. [online] Available at: <https://www.asf.alaska.edu/sentinel/data/image-quality/> [Accessed 20 Sep. 2016].

Arkett, M., Braithwaite, L., Pestieau, P., Carrieres, T., Pogson, L., Fabi, C. and Geldsetzer, T., 2015. Preparation by the Canadian Ice Service for the operational use of the RADARSAT Constellation Mission in their ice and oil spill monitoring programs. *Canadian Journal of Remote Sensing*, 41(5), pp.380–389.

Barber, D.G. and LeDrew, E.F., 1991. SAR sea ice discrimination using texture statistics : a multivariate approach. *Photogrammetric engineering and remote sensing*, 57(4), pp.385–395.

Berger, M., Moreno, J., Johannessen, J.A., Levelt, P.F. and Hanssen, R.F., 2012. ESA's sentinel missions in support of Earth system science. *Remote Sensing of Environment*, 120, pp.84–90.

Bintanja, R. and Selten, F.M., 2014. Future increases in Arctic precipitation linked to local evaporation and sea-ice retreat. *Nature*, 509(7501), pp.479–82.

Boykov, Y., Veksler, O. and Zabih, R., 2001. Fast approximate energy minimization via graph cuts. *IEEE Transactions on Pattern Analysis and Machine Intelligence*, 23(11), pp.1222–1239.

Breiman, L., 2001. Random forests. *Machine Learning*, 45(1), pp.5–32.

Breiman, L., Friedman, J., Stone, C.J. and Olshen, R.A., 1984. *Classification and Regression Trees*. CRC Press.

Canadian Coast Guard, 2012. *Ice Navigation in Canadian Waters*. Ottawa. Available at: <http://www.ccg-gcc.gc.ca/folios/00913/docs/ice-navigation-dans-les-galces-eng.pdf>

Canadian Ice Service, 2016. *About the Candian Ice Service*. [online] Available at: <http://www.ec.gc.ca/glaces-ice/default.asp?lang=En&n=955F6BE5-1> [Accessed 25 May 2016].

Casey, J.A., Howell, S.E.L., Tivy, A. and Haas, C., 2016. Separability of sea ice types from wide swath C- and L-band synthetic aperture radar imagery acquired during the melt season. *Remote Sensing of Environment*, 174, pp.314–328.

Cavalieri, D.J. and Parkinson, C.L., 2012. Arctic sea ice variability and trends, 1979-2010. *The Cryosphere*, 6(4), pp.881–889.

Clausi, D.A., 2001. Comparison and fusion of co-occurrence, Gabor and MRF texture features for classification of SAR sea-ice imagery. *Atmosphere-Ocean*, 39(3), pp.183–194.

Clausi, D.A., 2002. An analysis of co-occurrence texture statistics as a function of grey level quantization. *Canadian Journal of Remote Sensing*, 28(1), pp.45–62.

Clausi, D.A., Qin, A.K., Chowdhury, M.S., Yu, P. and Maillard, P., 2010. MAGIC: MAp-Guided Ice Classification System. *Canadian Journal of Remote Sensing*, 36(sup1), pp.S13–S25.

Congalton, R.G., 1991. A review of assessing the accuracy of classifications of remotely sensed data. *Remote Sensing of Environment*, 37(1), pp.35–46.

Dabboor, M. and Shokr, M., 2013. A new Likelihood Ratio for supervised classification of fully polarimetric SAR data: An application for sea ice type mapping. *ISPRS Journal of Photogrammetry and Remote Sensing*, 84, pp.1–11.

Delong, A., Osokin, A., Isack, H.N. and Boykov, Y., 2012. Fast approximate energy minimization with label costs. *International Journal of Computer Vision*, 96(1), pp.1–27.

Dey, D., Mummert, L. and Sukthankar, R., 2012. Classification of plant structures from uncalibrated image sequences. In: *2012 IEEE Workshop on the Applications of Computer Vision (WACV)*. IEEE, pp.329–336.

Dierking, W., 2010. Mapping of different sea ice regimes using images from Sentinel-1 and ALOS synthetic aperture radar. *IEEE Transactions on Geoscience and Remote Sensing*, 48(3), pp.1045–1058.

Eineder, M. and Bamler, R., 2014. *SAR Imaging*. Lecture at SAR-EDU, November 7, 2014. Available at: <https://saredu.dlr.de/unit/SAR_imaging>

Ellis, B. and Brigham, L., 2009. *Arctic Marine Shipping Assessment 2009 Report*. Arctic Coucil's Protection of the Arctic Marine Environment (PAME). Available at: <http://www.pmel.noaa.gov/arctic-zone/detect/documents/AMSA_2009_Report_2nd_print.pdf>

Environment and Climate Change Canada, 2016. Interpreting ice charts. [online] Available at: <https://www.ec.gc.ca/glaces-ice/default.asp> [Accessed 5 Jan. 2017]

European Space Agency, 2016. *Sentinel-1 SAR user guides*. [online] Available at:

<https://sentinel.esa.int/web/sentinel/user-guides/sentinel-1-sar/acquisition-modes/extra-wide-swath> [Accessed 25 Sep. 2016].

Fenty, I. and Heimbach, P., 2013. Coupled sea ice–ocean-state estimation in the Labrador Sea and Baffin Bay. *Journal of Physical Oceanography*, 43(5), pp.884–904.

Genuer, R., Poggi, J.-M. and Tuleau-Malot, C., 2016. *VSURF: Variable Selection Using Random Forests*. R package version 1.0.3. Available at: <http://CRAN.R-project.org/package=VSURF>

Genuer, R., Poggi, J. and Tuleau-Malot, C., 2010. Variable selection using random forests. *Pattern Recognition Letters*, 31(14), pp.2225–2236.

Geudtner, D., Torres, R., Snoeij, P., Davidson, M. and Rommen, B., 2014. Sentinel-1 System capabilities and applications. In: *IGARSS*. IEEE, pp.1457–1460.

Haralick, R.M., Shanmugam, K. and Dinstein, I., 1973. Textural Features for Image Classification. *IEEE Transactions on Systems, Man, and Cybernetics*, 3(6), pp.610–621.

Isleifson, D., Hwang, B., Barber, D.G., Scharien, R.K. and Shafai, L., 2010. C-band polarimetric backscattering signatures of newly formed sea ice during fall freeze-up. *IEEE Transactions on Geoscience and Remote Sensing*, 48(8), pp.3256–3267.

Karvonen, J., 2012. Baltic Sea ice concentration estimation based on C-band HH-polarized SAR data. *IEEE Journal of Selected Topics in Applied Earth Observations and Remote Sensing*, 5(6), pp.1874–1884.

Karvonen, J., 2014. Baltic Sea ice concentration estimation based on C-band dual-polarized SAR data. *IEEE Transactions on Geoscience and Remote Sensing*, 52(9), pp.5558–5566.

Karvonen, J., Gegiuc, A., Makynen, M. and Simila, M., 2015. *Sentinel-1 data for Operational Baltic and Arctic Sea ice monitoring at FMI*.

Kasapoglu, N.G., 2014. Sea ice concentration retrieval using composite ScanSAR features in a SAR data assimilation process. *IEEE Geoscience and Remote Sensing Letters*, 11(12), pp.2085–2089.

Kinnard, C., Zdanowicz, C.M., Fisher, D. a., Isaksson, E., de Vernal, A. and Thompson, L.G., 2011. Reconstructed changes in Arctic sea ice over the past 1,450 years. *Nature*, 479(7374), pp.509–512.

Kwok, R. and Rothrock, D.A., 2009. Decline in Arctic sea ice thickness from submarine and ICESat records: 1958-2008. *Geophysical Research Letters*, 36(15).

Kwon, T., Li, J. and Wong, A., 2013. ETVOS: An enhanced total variation optimization segmentation approach for SAR sea-ice image segmentation. *IEEE Transactions on Geoscience and Remote Sensing*, 51(2), pp.925–934.

Lang, W., Zhang, P., Wu, J., Shen, Y. and Yang, X., 2016. Incidence angle correction of SAR sea ice data based on locally linear mapping. *IEEE Transactions on Geoscience and Remote Sensing*, 54(6), pp.3188–3199.

Leigh, S., Wang, Z. and Clausi, D.A., 2014. Automated ice-water classification using dual polarization SAR satellite imagery. *IEEE Transactions on Geoscience and Remote Sensing*, 52(9), pp.5529–5539.

Li, F., Clausi, D.A., Wang, L. and Xu, L., 2015. A semi-supervised approach for ice-water classification using dual-polarization SAR satellite imagery. In: *2015 IEEE Conference on Computer Vision and Pattern Recognition Workshops (CVPRW)*. pp.28–35.

Malenovský, Z., Rott, H., Cihlar, J., Schaepman, M.E., García-Santos, G., Fernandes, R. and Berger, M., 2012. Sentinels for science: Potential of Sentinel-1, -2, and -3 missions for scientific observations of ocean, cryosphere, and land. *Remote Sensing of Environment*, 120, pp.91–101.

Moreira, A., 2013. Synthetic aperture radar (SAR): principles and applications. In: *4th Advanced Training Course in Land Remote Sensing*. ESA.

Morison, J., Kwok, R., Peralta-Ferriz, C., Alkire, M., Rigor, I., Andersen, R. and Steele, M., 2012. Changing Arctic Ocean freshwater pathways. *Nature*, 481(7379), pp.66–70.

National Snow and Ice Data Centre, 2016. *Daily image update*. [online] Available at: <http://nsidc.org/arcticseaicenews/2012/05/daily-image/> [Accessed 25 May 2016].

Nghiem, S. V., Kwok, R., Kong, J.A. and Shin, R.T., 1993a. A model with ellipsoidal scatterers for polarimetric remote sensing of anisotropic layered media. *Radio Science*, 28(5), pp.687–703.

Nghiem, S. V., Kwok, R., Yueh, S.H. and Drinkwater, M.R., 1995a. Polarimetric signatures of sea ice: 1. Theoretical model. *Journal of Geophysical Research*, 100(C7), pp.13665–13679.

Nghiem, S. V., Kwok, R., Yueh, S.H. and Drinkwater, M.R., 1995b. Polarimetric signatures of sea ice: 2. Experimental observations. *Journal of Geophysical Research*, 100(C7), pp.13681–13698.

Nghiem, S. V., Kwok, R., Yueh, S.H., Kong, J.A., Hsu, C.C., Tassoudji, M.A. and Shin, R.T., 1995c. Polarimetric scattering from layered media with multiple species of scatterers. *Radio Science*, 30(4), pp.835–852.

Nghiem, S. V., Yueh, S.H., Kwok, R. and Nguyen, D.T., 1993b. Polarimetric remote sensing of geophysical medium structures. *Radio Science*, 28(6), pp.1111–1130.

Nghiem, S.V. and Bertoia, C., 2001. Study of multi-polarization C-band backscatter signatures for Arctic sea ice mapping with future satellite SAR. *Canadian Journal of Remote Sensing*, 27(5), pp.387–402.

Nghiem, S.V., Kwok, R., Yueh, S.H., Kong, J.A., Tassoudji, M.A., Hsu, C.C., Gow, A.J. and Perovich, D.I., 1994. Polarimetric backscattering signatures from thin saline ice under controlled laboratory conditions. In: *1994 IEEE International Geoscience and Remote Sensing Symposium*. pp.611–613.

Notz, D. and Stroeve, J., 2016. Observed Arctic sea-ice loss directly follows anthropogenic CO2 emission. *Science*, 354(6313), pp.747–750.

Ochilov, S. and Clausi, D.A., 2012. Operational SAR Sea-Ice Image Classification. *IEEE Transactions on Geoscience and Remote Sensing*, 50(11), pp.4397–4408.

Office of the Auditor General of Canada, 2014. Marine Navigation in the Canadian Arctic. In: *2014 Fall Report of the Commissioner of the Environment and Sustainable Development*. Available at: <http://www.oag-bvg.gc.ca/internet/English/parl_cesd_201410_03_e_39850.html>

Post, E., Bhatt, U.S., Bitz, C.M., Brodie, J.F., Fulton, T.L., Hebblewhite, M., Kerby, J., Kutz, S.J., Stirling, I. and Walker, D.A., 2013. Ecological consequences of sea-ice decline. *Science*, 341(6145), pp.519–524.

Qin, A.K. and Clausi, D.A., 2010. Multivariate image segmentation using semantic region growing with adaptive edge penalty. *IEEE Transactions on Image Processing*, 19(8), pp.2157–2170.

Ramsay, B., Hirose, T., Manore, M., Falkingham, J., Gale, R., Barber, D., Shokr, M., Danielowicz, B., Gorman, B. and Livingstone, C., 1993. Potential of RADARSAT for sea ice applications. *Canadian Journal of Remote Sensing*, 19(4), pp.352–362.

Ressel, R., Frost, A. and Lehner, S., 2015. A neural network-based classification for sea ice types on X-band SAR images. *IEEE Journal of Selected Topics in Applied Earth Observations*

and Remote Sensing, 8(7), pp.3672–3680.

Richards, J.A., 2009. *Remote sensing with imaging radar*. Springer Berlin Heidelberg.

Scheuchl, B., Flett, D., Caves, R. and Cumming, I., 2004. Potential of RADARSAT-2 data for operational sea ice monitoring. *Canadian Journal of Remote Sensing*, 30(3), pp.448–461.

Screen, J. a and Simmonds, I., 2010. The central role of diminishing sea ice in recent Arctic temperature amplification. *Nature*, 464(7293), pp.1334–1337.

Serreze, M.C., Holland, M.M. and Stroeve, J., 2007. Perspectives on the Arctic's shrinking sea-ice cover. *Science*, 315(5818), pp.1533–1536.

Siva, P. and Wong, A., 2014. URC: Unsupervised regional clustering of remote sensing imagery. In: *IGARSS*. pp.4938–4941.

Soh, L.-K. and Tsatsoulis, C., 1999. Texture analysis of SAR sea ice imagery using gray level co-occurrence matrices. *IEEE Transactions on Geoscience and Remote Sensing*, 37(2), pp.780–795.

Tan, W., Liao, R., Du, Y., Lu, J. and Li, J., 2015. Improving urban impervious surface classification by combining Landsat and PolSAR images: A case study in Kitchener-Waterloo, Ontario, Canada. In: *IGARSS*. pp.1917–1920.

Taylor, R., Turnbull, I. and Slaney, A., 2015. Field data for sea ice and iceberg drift offshore Newfoundland and Labrador. In: *OTC Arctic Technology Conference*. Offshore Technology Conference, pp.1–7.

Torres, R., Snoeij, P., Geudtner, D., Bibby, D., Davidson, M., Attema, E., Potin, P., Rommen, B., Floury, N., Brown, M., Traver, I.N., Deghaye, P., Duesmann, B., Rosich, B., Miranda, N., Bruno, C., L'Abbate, M., Croci, R., Pietropaolo, A., Huchler, M. and Rostan, F., 2012. GMES Sentinel-1 mission. *Remote Sensing of Environment*, 120, pp.9–24.

Veksler, O. and Delong, A., 2010. *GCoptimization - software for energy minimization with graph cuts*. Version 3.0. Available at: <http://www.csd.uwo.ca/faculty/olga/software.html>

Walsh, J.E., Fetterer, F., Scott, S.J. and Chapman, W.L., 2016. A database for depicting Arctic sea ice variations back to 1850. *Geographical Review*, pp.1–20.

Wang, L., Scott, K.A. and Clausi, D.A., 2016. Improved sea ice concentration estimation through fusing classified SAR imagery and AMSR-E data. *Canadian Journal of Remote Sensing*, 42(1), pp.41–52.

Wang, L., Scott, K.A., Xu, L. and Clausi, D.A., 2016. Sea ice concentration estimation during

melt from dual-pol SAR scenes using deep convolutional neural networks: A case study. *IEEE Transactions on Geoscience and Remote Sensing*, 54(8), pp.4524–4533.

Wang, M. and Overland, J.E., 2012. A sea ice free summer Arctic within 30 years: An update from CMIP5 models. *Geophysical Research Letters*, 39(18), pp.1–5.

Weeks, W.F. and Ackley, S.F., 1982. The growth, structure, and properties of sea ice. *CRREL monograph 82-1*, pp.9–164.

Xu, K., Yang, W., Liu, G. and Sun, H., 2013. Unsupervised satellite image classification using Markov field topic model. *IEEE Geoscience and Remote Sensing Letters*, 10(1), pp.130–134.

Xu, L., Li, J. and Brenning, A., 2014. A comparative study of different classification techniques for marine oil spill identification using RADARSAT-1 imagery. *Remote Sensing of Environment*, 141, pp.14–23.

Xu, L., Li, J., Wong, A. and Wang, C., 2014. A KPCA texture feature model for efficient segmentation of RADARSAT-2 SAR sea ice imagery. *International Journal of Remote Sensing*, 35(13), pp.5053–5072.

Yan, J., Shan, J. and Jiang, W., 2014. A global optimization approach to roof segmentation from airborne lidar point clouds. *ISPRS Journal of Photogrammetry and Remote Sensing*, 94, pp.183–193.

Yu, P., Clausi, D.A. and Qin, A.K., 2012. Feature extraction of dual-pol SAR imagery for sea ice image segmentation. *Canadian Journal of Remote Sensing*, 38(3), pp.352–366.

Yu, Q. and Clausi, D.A., 2008. IRGS: Image segmentation using edge penalties and region growing. *IEEE Transactions on Pattern Analysis and Machine Intelligence*, 30(12), pp.2126–2139.

Zakhvatkina, N.Y., Alexandrov, V.Y., Johannessen, O.M., Sandven, S. and Frolov, I.Y., 2013. Classification of sea ice types in ENVISAT synthetic aperture radar images. *IEEE Transactions on Geoscience and Remote Sensing*, 51(5), pp.2587–2600.

De Zan, F. and Guarnieri, A.M., 2006. TOPSAR: Terrain observation by progressive scans. *IEEE Transactions on Geoscience and Remote Sensing*, 44(9), pp.2352–2360.

Zvoleff, A., 2016. *glcm: Calculate Textures from Grey-Level Co-Occurrence Matrices (GLCMs)*. R package version 1.6.1. Available at: <http://CRAN.R-project.org/package=glcm>.

Appendix A

Ice chart on January 18

Interpretation of egg codes (Environment and Climate Change Canada (EC), 2016)
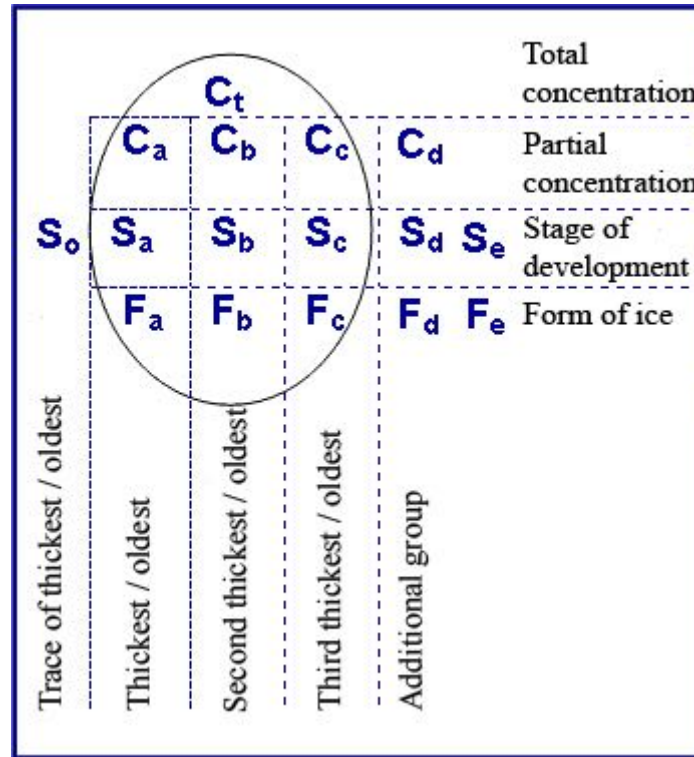
Three basic data about sea ice: concentration, stage of development and form of ice, and these data were recorded in an oval in an ice chart. The oval and the coding associated with it are called "egg code". The first row defines the total concentration (C_t) of ice in the polygon, recorded in tenths, and the second row records partial concentration of the thickest (C_a), second thickest (C_b), and third thickest (C_c) ice in tenths. The third row defines the stages of development of corresponding ice types (S_a, S_b, S_c), while the fourth row defines the forms of ice (F_a, F_b, F_c). When more than three types of ice are present, additional ice information can be added on the right side. If there's a trace (thicker than S_a but has concentration less than 1/10) present, it is recorded as S_0. The numeric codes for the stage of development and form of ice are shown in the two tables below.

Code for stage of development in this thesis (adapted from (GC, 2016))

Description	Thickness	Code
New ice	< 10 cm	1
Grey Ice	10 - 15 cm	4
Grey-white ice	15 - 30 cm	5
Thin first-year ice	30 - 70 cm	7
Medium first-year ice	70 - 120 cm	1·
Ice of land origin	-	▲·
Undetermined or unknown	-	X·

Code for form of ice in this thesis (adapted from (GC, 2016))

Description	>Width	Code
Small floe	20 - 100 m	3
Medium floe	100 - 500 m	4
Big floe	500 - 2,000 m	5
Vast floe	2 - 10 m	6
Fast ice	-	8
Icebergs, growlers or floebergs	-	9
Undetermined, unknown or no form	-	X

Appendix B

Noise floor of RADARSAT-2 (HV)
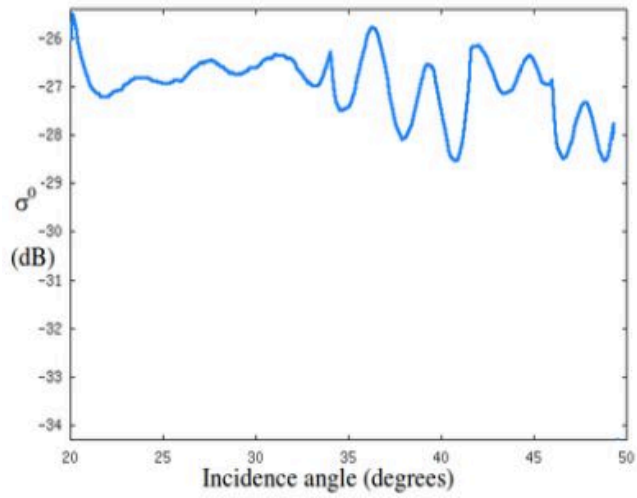
Observed noise floor of Sentinel-1 (HV)
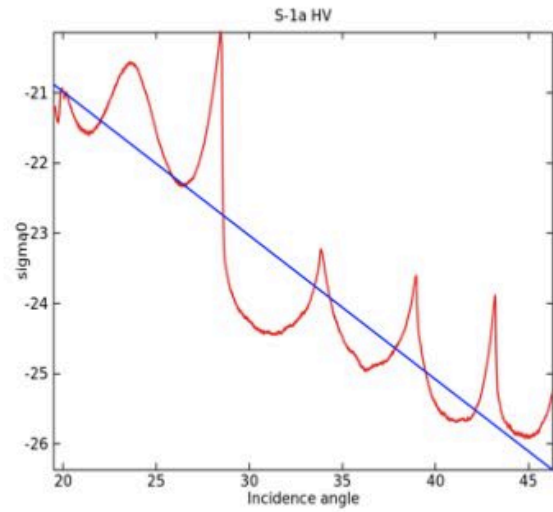
Noise floor comparison of RADARSAT-2 ScanSAR Wide and Sentinel-1 EW in HV (Karvonen et al., 2015)

Appendix C

Results of Image Segmentation

Left: segmentation result   Middle: RGB image of data   Right: reference map of water
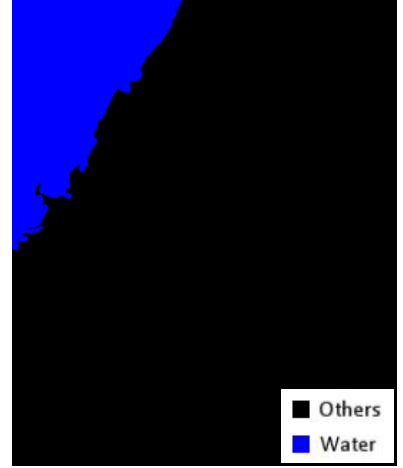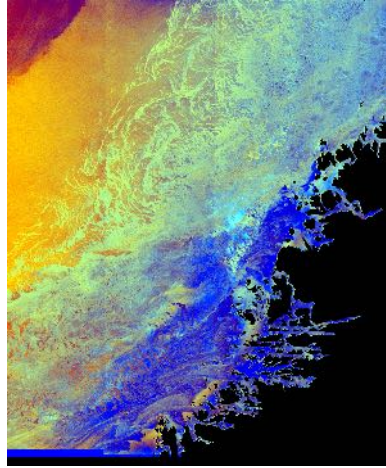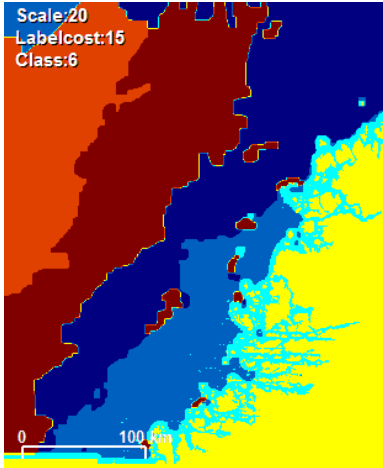
Scene: January 4; UA:75.4%; PA: 83.6%; OA: 94.7%
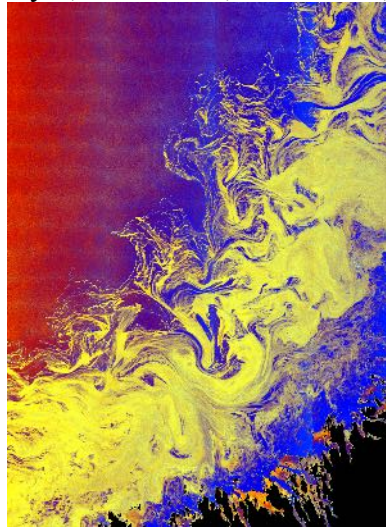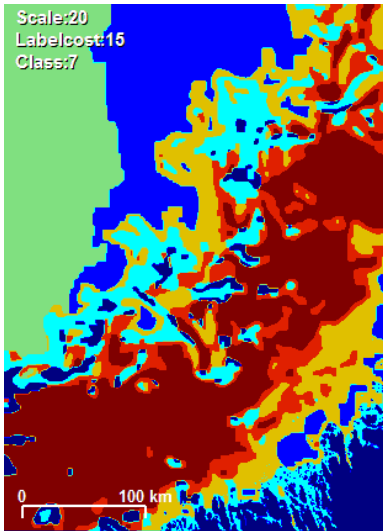
Scene: January 11; UA:90.1%; PA: 96.6%; OA: 96.0%
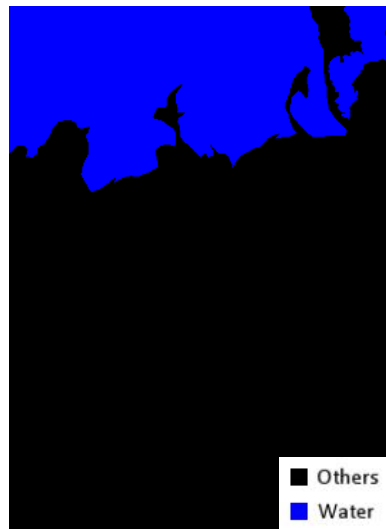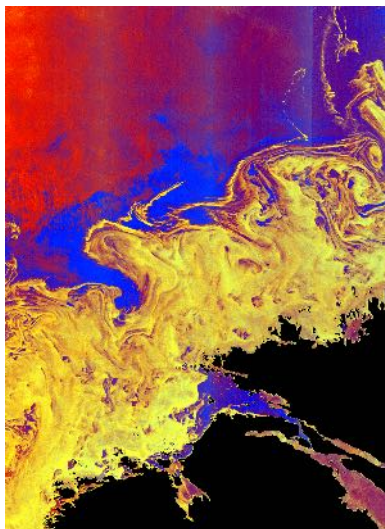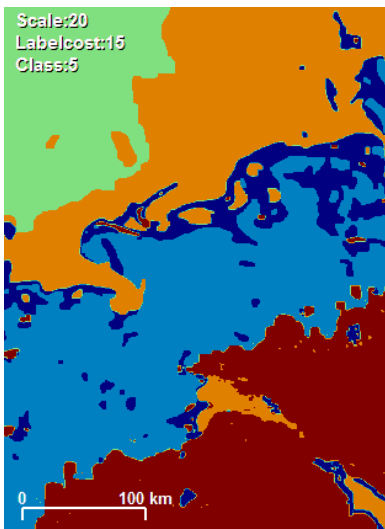
Scene: January 18; UA:61.8%; PA: 99.8%; OA: 85.4%
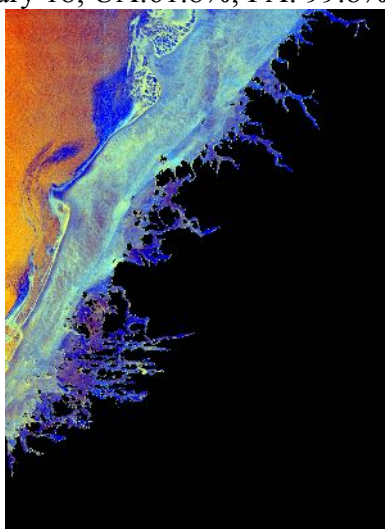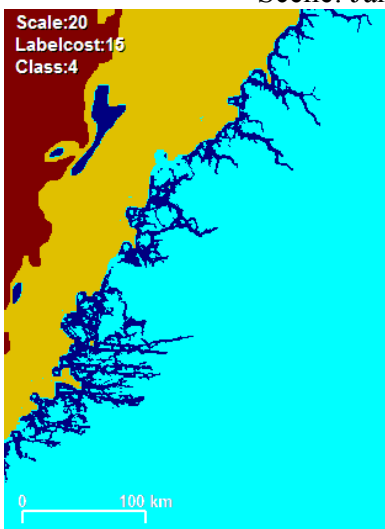
Scene: January 21; UA:85.3%; PA: 91.2%; OA: 97.9%
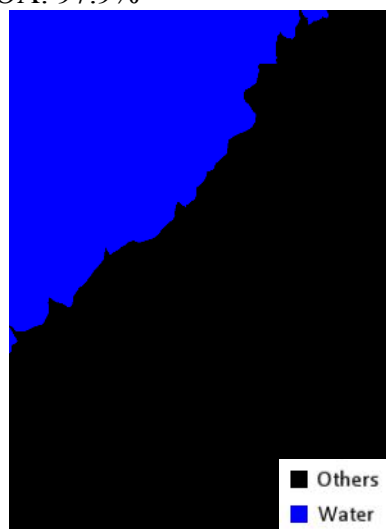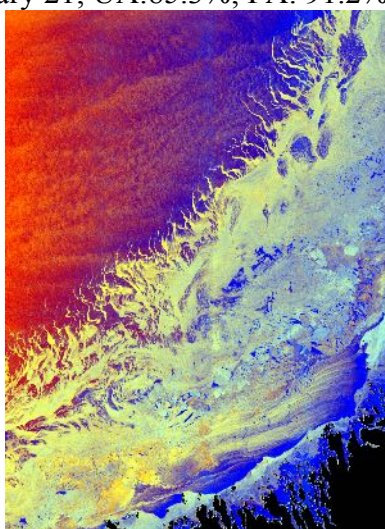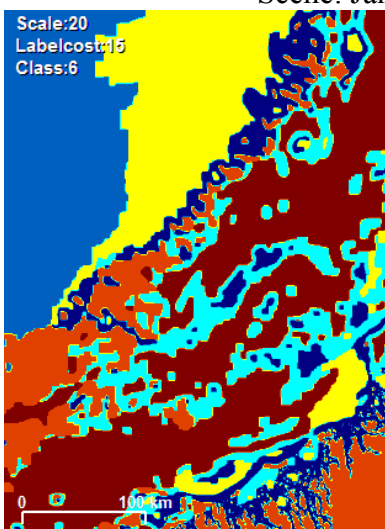
Scene: February 4; UA:88.3%; PA: 99.4%; OA: 96.0%
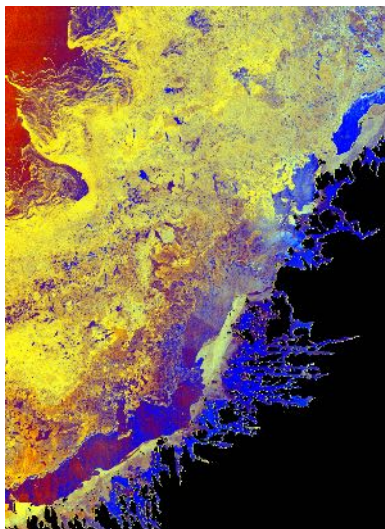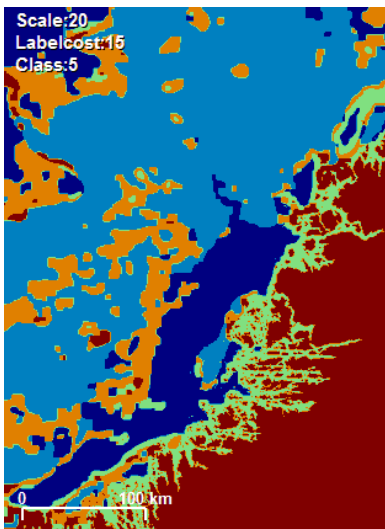
Scene: March 16; UA:14.2%; PA: 88.2%; OA: 86.9%
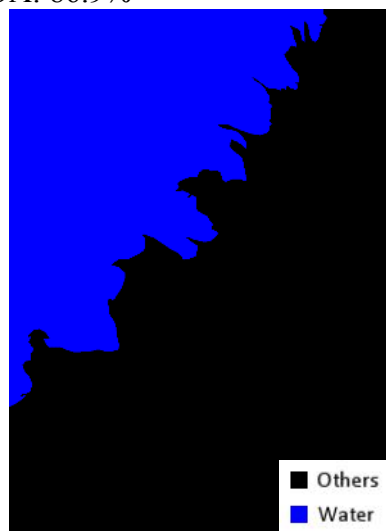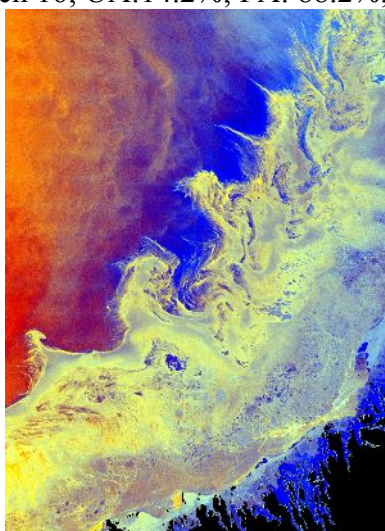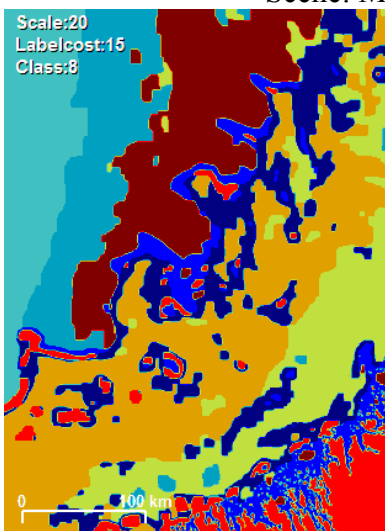
Scene: March 23; UA:95.3%; PA: 95.9%; OA: 97.0%
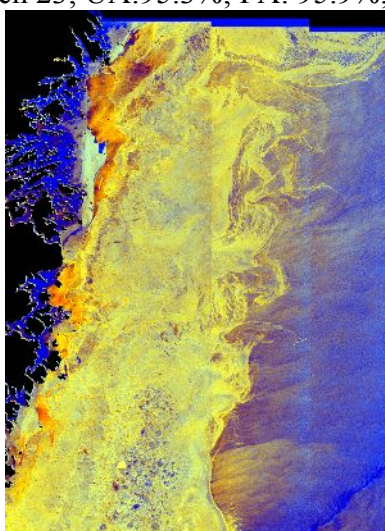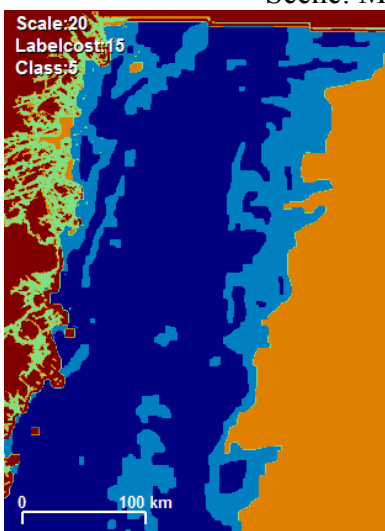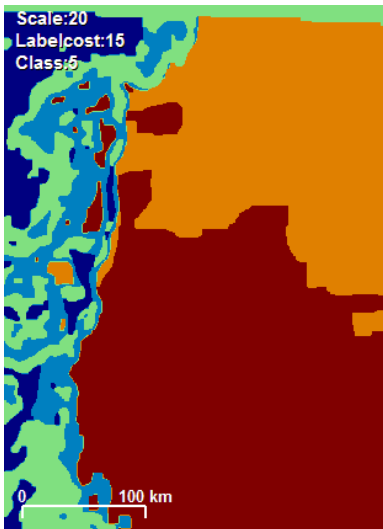

Scene: April 2; UA:97.6%; PA: 86.9%; OA: 95.8%
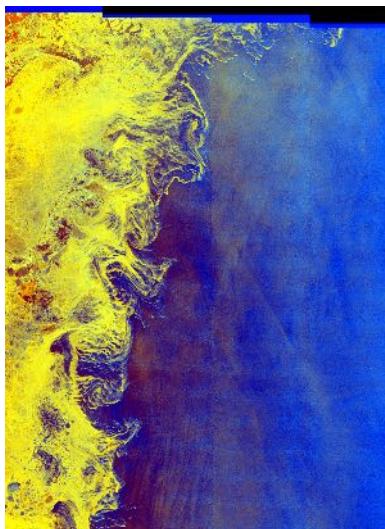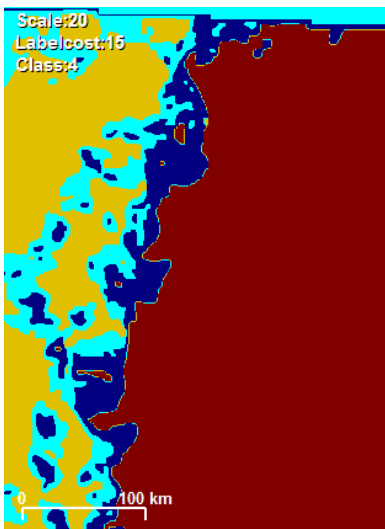
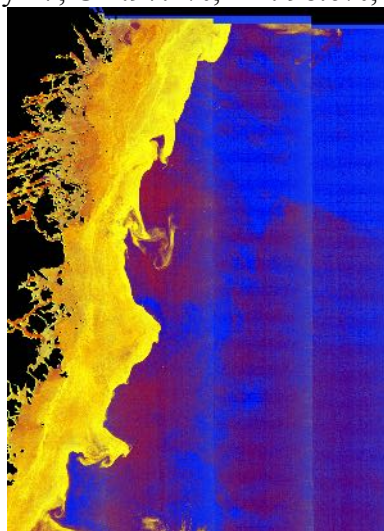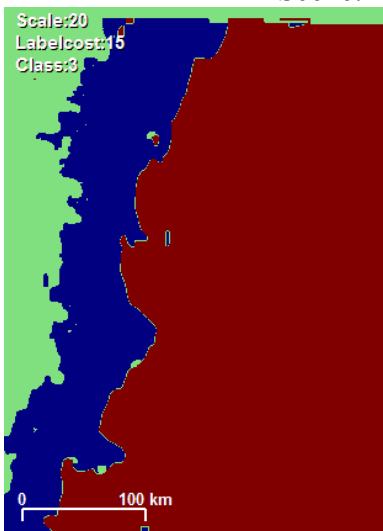Scene: April 9; UA:96.7%; PA: 98.7%; OA: 97.4%
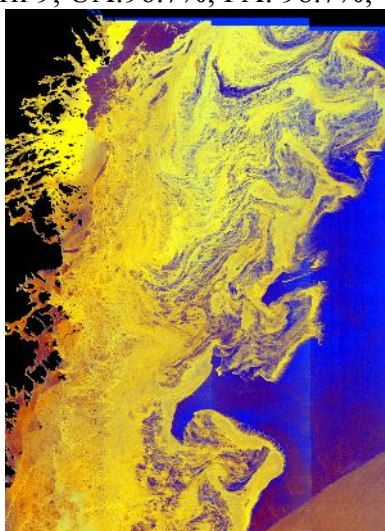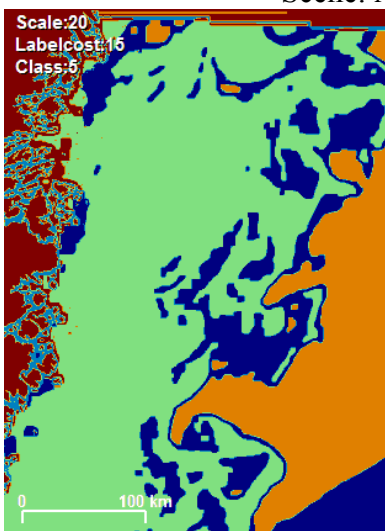
Scene: April 26; UA:88.7%; PA: 84.2%; OA: 95.2%
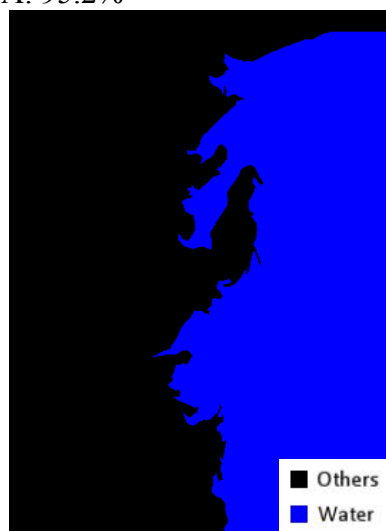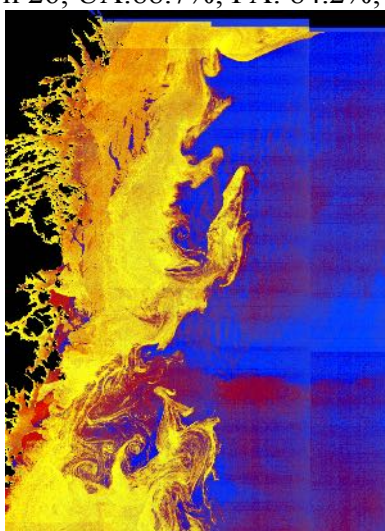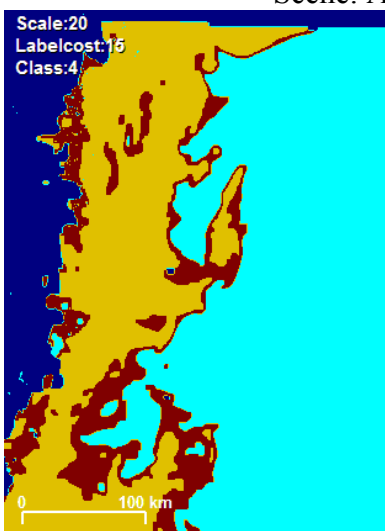
Scene: May 20; UA:90.9%; PA: 99.6%; OA: 95.4%
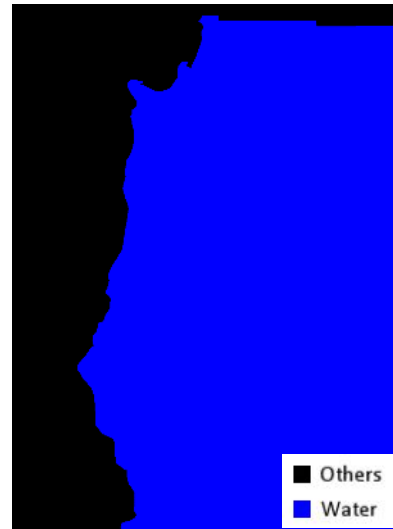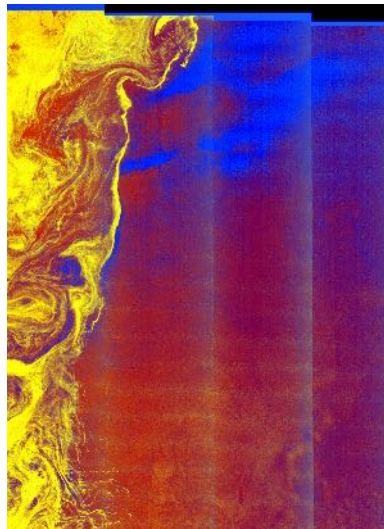
Scene: May 27; UA:97.1%; PA: 98.6%; OA: 97.0%

Scene: June 13; UA:97.8%; PA: 99.5%; OA: 98.3%

UA: user's accuracy; PA: producer's accuracy; OA: overall accuracy